p70S6 kinase-dependent phosphorylation of the μ2 subunit of the AP2 adaptor complex is needed for clathrin-mediated endocytosis.

Aleksandra Tempes[1,2*], Agnieszka Brzozowska[1,*], Tomasz Węgierski[3], Katarzyna Olek[4], Kamil Jastrzębski[5], Ewa Liszewska[1], Katarzyna Misztal[3], Katarzyna Machnicka[1], Matylda Macias[3], Aleksandra Szybińska[3], Ewa Sitkiewicz[6], Agata Gozdz[1,7], Antoni G. Wróbel[8], Marta Miaczynska[5], Wojciech Pokrzywa[4], Jacek Jaworski[1,$], Anna R Malik[1,2,$]

[1] – Laboratory of Molecular and Cellular Neurobiology, International Institute of Molecular and Cell Biology in Warsaw, Warsaw, Poland

[2] – Cellular Neurobiology Research Group, Faculty of Biology, University of Warsaw, Warsaw, Poland

[3] – IN-MOL-CELL Microscopy Facility, International Institute of Molecular and Cell Biology in Warsaw, Warsaw, Poland

[4] – Laboratory of Protein Metabolism, International Institute of Molecular and Cell Biology in Warsaw, Warsaw, Poland

[5] – Laboratory of Cell Biology, International Institute of Molecular and Cell Biology in Warsaw, Warsaw, Poland

[6] – Laboratory of Mass Spectrometry, Institute of Biochemistry and Biophysics, Polish Academy of Sciences, Warsaw, Poland

[7] – Department of Histology and Embryology, Center of Biostructure Research, Medical University of Warsaw, ul. T. Chałubińskiego 5, 02-004 Warsaw, Poland

[8] – Department of Biochemistry, University of Oxford, South Parks Road, Oxford, UK

* – equal contribution

$ – corresponding authors

Abstract

Clathrin-mediated endocytosis (CME) is a process in which ligands and their corresponding receptors at the cell surface are internalized via clathrin-coated invaginations of the plasma membrane. Both clathrin and endocytic cargo are recruited to the clathrin-coated pit by the adaptor protein complex AP2. AP2 resides in the cytoplasm in the closed conformation and opens upon interacting with the plasma membrane. Effective CME requires both pools of AP2, open and closed, and effective transition between these states but the mechanisms regulating this transition are only partially understood. Here, we report that serine 45 (S45) of the μ2 subunit of the AP2 complex is phosphorylated in a p70S6 kinase-dependent manner in HeLa cells both with hyperactivated mTOR signaling and under basal conditions. We demonstrate that the loss of S45-μ2 phosphorylation results in decreased internalization of canonical CME cargo such as transferrin and PDGF receptors. In *Caenorhabditis elegans*, the absence of S45-μ2 phosphorylation produces the dumpy phenotype characteristic of the loss of function of AP2. Our live imaging experiments further suggest that these phenotypes might arise because S45-μ2 phosphorylation is needed for conformational changes of the AP2 complex. These findings uncover a mechanism central to CME control and extend our knowledge on the role of post-translational modifications of AP2 components in regulating the function of this complex.

Keywords: clathrin-mediated endocytosis, accessory protein complex 2, AP2 conformational change, AP2 phosphorylation, p70S6K

Introduction

The intracellular environment of mammalian cells is protected from the extracellular environment by the plasma membrane which is impermeable to hydrophilic molecules. Because of this strict protection, specialized mechanisms such as endocytosis need to be utilized for the uptake of

molecules critical for proper cell function. Among various types of endocytosis, clathrin-mediated endocytosis (CME) is the most intensively studied due to its key role in development, physiology, and its involvement in diseases such as neurodegeneration and cancer [1,2]. During CME, cargo is internalized from the plasma membrane via so-called clathrin-coated pits (CCPs) either constitutively (e.g., transferrin receptor, TrfR) or exclusively upon ligand binding (e.g., platelet derived growth factor receptor, PDGFR). CCPs are invaginations of the plasma membrane enriched with the cargo destined for internalization. They are covered with a clathrin lattice, which shapes CCPs into clathrin-coated vesicles (CCVs) that transport the cargo through the intracellular space [3].

However, clathrin on its own cannot bind either cargo or the plasma membrane. Therefore, for CME to take place, the adaptor protein complex AP2 is utilized, which simultaneously binds to the plasma membrane, cargo, and clathrin [1,2]. AP2 consists of four subunits: two large ones (α and β2 [~ 110 kDa]), medium μ2 (50 kDa), and small σ2 (17 kDa). While all four constitute the core of AP2, the α and β2 subunits extend the hinge and appendage domains (or α- and β2-ears) beyond the core. The α, β2, and μ2 subunits recognize phosphatidylinositol 4,5-bisphosphate (PIP2) and are therefore responsible for AP2 binding to the plasma membrane [2,3]. Finally, the μ2 and σ2 acting together with α subunit bind cargo possessing Yxxφ and dileucine motifs, respectively. The AP2 core can adopt several different conformations including closed, open, and open+ [1,2,4–7]. In the closed conformation, μ2 and β2 domains, responsible for binding cargo and clathrin, respectively, are inaccessible. Upon binding PIP2 at the plasma membrane, AP2 opens to bind cargo and clathrin.

CME is strictly controlled, and many key endocytic proteins are phosphorylated at some point [8,9]. Endocytosis-regulating phosphorylation can affect CME progress either positively or

negatively [8,9]. Phosphorylation of μ2 at threonine 156 (T156) is the most extensively studied one but its exact function is still debated [7,10–12]. Of note, according to PhosphoSitePlus (https://www.phosphosite.org), 16 additional serine or threonine phosphorylation sites were detected in μ2 by mass spectrometry. Of them, only the role of serine 45 (S45) phosphorylation was partially characterized, suggesting its negative role in the internalization of the transient receptor potential cation channel subfamily V member 1 (TRPV1) [13].

p70S6 kinase (p70S6K) is best known for its role in the regulation of protein synthesis. Its functions are mostly studied in the context of mTORopathies, a group of diseases resulting from excessive activity of the mTOR kinase and its downstream targets including p70S6K [14,15]. In most cases, mTOR overactivation is caused by inactivating mutations of its key regulators, *TSC1* or *TCS2* encoding hamartin and tuberin, respectively. Recent phosphoproteomics data have revealed hundreds of proteins phosphorylated in a p70S6K-dependent manner, pointing to its role in regulating a variety of cellular processes in addition to translation, including control of protein folding, RNA splicing, nucleotide synthesis, cytoskeleton dynamics, and membrane trafficking [16–18]. Of note, pharmacological inhibition or knockdown of p70S6K led to decreased rates of albumin endocytosis and less efficient formation of CCVs in opossum kidney proximal tubule cells [19]. However, whether the role of p70S6K in CME regulation is conserved between species and cell types, and the molecular basis of its involvement remains largely unknown. Therefore, in this study, we used different cargo uptake assays, live imaging of CCP formation, and mass spectrometry to test the hypothesis of the critical involvement of p70S6K in CME regulation in human cells. As a result, we showed that the activity of p70S6K is needed for CME cargo uptake. This results from p70S6K-dependent phosphorylation of S45 of μ2, which is likely essential for both AP2 cargo binding and effective formation of CCPs.

Results

Cargo internalization via CME is upregulated in cells with increased p70S6K activity.

Evidence exists for a p70S6K contribution to CCV formation in very specialized cells (proximal tubular cells) [19], but it is unclear if and how p70S6K affects this type of endocytosis in other cell types. Therefore, we first looked at CME in cells with increased p70S6K activity due to loss of hamartin (for review see: [15,20,21]). First, we generated HeLa cell lines stably expressing shRNA targeting *TSC1* mRNA ($HeLa^{shTSC1}$) and GFP-tagged clathrin light chain (EGFP-CLCa) to enable further detailed analysis of CCPs formation. As a control, we generated $HeLa^{WT}$ cell line expressing EGFP-CLCa. Constitutive overexpression of shTSC1 resulted in an almost complete loss of hamartin (**Fig. 1A, B**) and, as anticipated, an increase in phosphorylation of the direct target of p70S6K, ribosomal protein S6 (P-S6, Ser235/236), confirming the activation of p70S6K (**Fig. S1A, B**). Next, we tested whether the knockdown of *TSC1* affects the early steps of the CME by analyzing the uptake of fluorescently labeled transferrin. Transferrin uptake occurs via the transferrin receptor (TrfR, aka TfR, Trfr), a canonical CME cargo. Cells with decreased *TSC1* expression and overactivation of p70S6K showed an increased uptake of transferrin compared to control cells (**Fig. 1C, D**). Pretreatment of the cells with a p70S6K inhibitor (p70S6Ki) clearly prevented the increased transferrin uptake induced by *TSC1* knockdown (**Fig. 1C, D**), substantiating the notion that the activity of p70S6K is critical for enhanced CME seen in $HeLa^{shTSC1}$.

Next, we looked for the causes of the difference in transferrin uptake between $HeLa^{WT}$ and $HeLa^{shTSC1}$ cells. First, we investigated whether lower levels of surface TrfR could explain the decreased transferrin uptake. Western blot analysis of membrane protein fraction obtained from $HeLa^{WT}$ and $HeLa^{shTSC1}$ cells using the cell surface biotinylation assay revealed no significant

reduction of TrfR cell surface levels (**Fig. 1E, F**). The silencing of *TSC1* also did not affect the amounts of AP2 complex subunits (**Fig. 1G, H**). Therefore, we tested whether the increased internalization of transferrin might be due to the regulatory effects of p70S6K on the dynamics of the early steps of the CME. To test this hypothesis, we performed an analysis of CCV formation using total internal reflection fluorescence (TIRF) microscopy based on the behavior of the GFP-tagged clathrin light chain (EGFP-CLCa). TIRF microscopy allows visualization of clathrin-coated pits (CCPs) at the cell membrane and measurement of the parameters describing all steps of CCP formation: nucleation, initiation, growth, and maturation [22–24]. More specifically, we analyzed the number of clathrin structures (CSs) and CCPs, the rate of clathrin polymerization, and finally the lifetime of CCPs. CSs are short-lived (up to 15 s) and dim structures, which never reach maturation and in consequence are aborted. In contrast, mean lifetime of CCPs is >20 s to even 2-3 minutes and their fluorescence, reflecting clathrin recruitment, increases during maturation and then decreases due to scission from the plasma membrane [25,26]. A high number of CSs exceeding the number of CCPs may be a sign that CCP initiation is frequent but fails to proceed to the mature state, for example due to improper recruitment of adaptor proteins. In contrast, a high number of CCPs relative to total clathrin structures may indicate productive and efficient endocytosis. The rate of clathrin polymerization, measured as the slope of EGFP-CLCa fluorescence intensity curve at the initial growth phase, provides information about the speed of clathrin incorporation into nascent CCP. The speed of clathrin incorporation is critical to the entire process of CME: too slow recruitment results in the abortion of the forming CCP [3]. Moreover, the differences in EGFP-CLCa signal intensities at the starting point give information about the initial size of forming CCP [25]. Finally, a comparison of the numbers of short- and long-lived CCPs informs about assembly, stability, and general progress of endocytosis. The results of our

analysis indicated important differences in the dynamics of CCPs formation between HeLa^{shTSC1} and control cells. Thus, in HeLa^{shTSC1} cells we observed more bona fide CCPs and fewer CSs than in control cells (**Fig. 1I**). Moreover, the starting point for EGFP fluorescence in HeLa^{shTSC1} cells was higher when compared to control cells **(Fig. 1J**), which suggests that the CCPs are bigger. We also observed a significant increase in the fraction of short-lived CCPs (below 40 s) and a decrease in long-lived CCPs (above 40s) in cells with *TSC1* depletion (**Fig. 1K, L**). Not all CCPs go through the whole life cycle: even 30-50 % of short-lived CCPs fail to mature [27], but HeLa^{shTSC1} cells internalized transferrin more efficiently than control cells, which suggests that a fraction of those short-lived CCPs is fully functional in these cells. This could also provide an explanation for the higher amount of CCPs in those cells when compared to control cells. Altogether, our TIRF microscopy analysis suggests that in cells with lowered *TSC1* expression and p70S6K overactivation, the whole process of CME is more efficient compared to the cells with normal levels of hamartin.

Knowing that increased p70S6K activity in HeLa^{shTSC1} cells enhances the CME of TrfR, we sought to determine whether this effect is consistent in other cell types and with other cargo. To this end, we analyzed PDGFR internalization [28] in CCD-1070Sk fibroblasts stimulated with its ligand PDGF. As before in HeLa cells, we depleted these cells of hamartin to drive overactivation of the mTOR-p70S6K signaling. Towards this end, we used lentiviral delivery of shTSC1 to generate CCD-1070Sk^{shTSC1} cells while the control cells received the pLKO vector (**Fig. 1M, N)**. As in the transferrin uptake in HeLa cells described above, CCD-1070Sk cells with overactive p70S6K (**Fig. 1M, N**) endocytosed significantly more PDGFR than control cells upon PDGF treatment (**Fig. 1O, P)** as revealed by immunofluorescence intensity analysis for internalized PDGFR. As expected, the endocytosed PDGFR colocalized with EEA1, a marker of

early endosomes. At the same time, the total PDGFR level remained unchanged compared with control cells, while P-S6 was increased (**Fig. 1M, N**). Like in the case of TrfR endocytosis in HeLa cells, increased PDGFR internalization in CCD-1070Sk^{shTSC1} cells was blocked by pretreatment with p70S6K inhibitor (**Fig. 1O, P**). Overall, we concluded that p70S6K is responsible for the upregulation of early CME steps in cells with *TSC1* knockdown, both in the case of TrfR internalization in HeLa cells and PDGFR endocytosis in fibroblasts.

Efficient CME requires p70S6K activity in cells with basal mTOR activity.

Our discovery that p70S6K is involved in enhanced cargo uptake via CME in cells with hyperactive mTOR prompted us to check if the same holds true in cells with intact *TSC1*. Towards this end, we performed the transferrin uptake assay in HeLa cells with reduced expression of the μ2 encoding gene *AP2M1* (HeLa KO μ2) [29] transfected with a plasmid encoding myc-μ2^{WT} [30] along with EGFP to label the transfected cells and visualize their morphology. An analogous approach, i.e. replacement of endogenous μ2 with exogenous one, was used in the work of Kadlecova et al. (2017) [3], as it allows a more accurate comparison of the effects of mutations in μ2 on the progression of CME and a better insight into the stage of impairment of AP2 functions. Obtained μ2^{WT} cells were kept serum-starved before the addition of p70S6K inhibitor or DMSO (negative control), and then transferrin internalization was measured as described above for HeLa^{shTSC1}. Treatment with p70S6Ki decreased P-S6 levels compared with control cells, confirming its efficacy **(Fig. 2A, B)**. The amount of internalized transferrin was also lower after treatment with p70S6Ki (**Fig. 2C, D**). However, reduced transferrin uptake was not due to decreased TrfR levels, as determined by Western blotting and immunofluorescence (**Fig. 2A, B, E, F**). We also tested whether inhibition of p70S6K activity affected the levels of transferrin binding to the cell surface, as an estimate of the TrfR presence. To this end, we treated μ2^{WT} cells

with p70S6Ki as described above and assessed the levels of fluorescently labeled transferrin bound to the cell membrane. As a result, we observed a slightly increased transferrin fluorescence on the cell surface in $\mu2^{WT}$ cells treated with p70S6Ki. Thus, decreased transferrin internalization in cells treated with p70S6Ki is not an effect of the lower amount of TrfR on the cell surface (**Fig. 2G, H**). p70S6Ki treatment also did not affect the levels of overexpressed myc-$\mu2^{WT}$ and the endogenous β2 subunit, ruling out the possibility that the differences in transferrin uptake were due to unequal AP2 levels (**Fig. 2A, B**). Thus, we conclude that the p70S6Ki treatment of HeLa cells results in decreased internalization of TrfR. To extend our observation to other cells and cargoes, we checked whether endocytosis of the PDGFR in wild-type CCD-1070Sk fibroblasts also depends on intact p70S6K activity. Indeed, p70S6Ki treatment resulted in a significant decrease in internalized PDGFR after PDGF stimulation (**Fig. 2I, J**). At the same time, p70S6Ki completely blocked the phosphorylation of S6 protein, while the total PDGFR level barely changed compared with control cells (**Fig. 2K, L**). Thus, we conclude that inhibition of p70S6K blocks CME, and this effect is universally seen for different cell types and cargoes.

p70S6K indirectly regulates μ2 phosphorylation.

Given the results described above and the potential regulatory role of μ2 phosphorylation in CME progression, we checked whether μ2 phosphorylation is sensitive to the p70S6K inhibitor. To this end, we performed tandem MS analysis of GFP-Avi-tag-μ2 overexpressed in serum-deprived HEK293T cells treated with p70S6Ki or DMSO (as control). Compared to control, inhibition of p70S6K resulted in loss of phosphorylation at four μ2 amino acid residues: serine 45 (S45), threonine 53, serine 61 and serine 309 (**Fig. 3A**). Although our MS analysis revealed four p70S6Ki-sensitive residues, only phosphorylation of S45 was confirmed in the PhosphoSite Plus database at the time of our analysis and was therefore selected for further studies. Thus, we tested

whether p70S6K phosphorylates μ2 directly. The results of the *in vitro* ^{33}P radioisotope kinase activity assay using commercially available recombinant p70S6K and purified GST-tagged fragment of μ2^{WT} (amino acids 1 to 156, GST-μ2$^{WT(aa1-156)}$), μ2$^{S45A(aa1-156)}$ (mutant that cannot be phosphorylated at the S45 residue), or the C-terminal part of RPS6 (positive control) did not confirm this possibility (**Fig. 3B**). We also checked whether wild-type p70S6K produced in HEK293T cells acquires the ability to phosphorylate GST-μ2$^{WT(aa1-156)}$, but again we did not detect phosphorylation of μ2 (**Fig. 3C**). At the same time, our positive control was phosphorylated by wild-type p70S6K, but not by its kinase-dead version (KD [K100R]) (**Fig. 3C**). Overall, our results suggest that μ2 is rather not a direct substrate for p70S6K. Still, the activity of p70S6K is required for S45-μ2 phosphorylation. Therefore, we decided to further explore the functional links between p70S6K activity, S45-μ2 phosphorylation and the regulation of CME, and to test whether the absence of S45-μ2 phosphorylation mimics the effects of p70S6K inhibition on CME.

Lack of S45-μ2 phosphorylation mimics the effects of p70S6K inhibition on transferrin internalization.

To further investigate the possibility that p70S6K activity affects CME by controlling S45-μ2 phosphorylation, we tested whether the absence of this posttranslational modification has similar effects as the use of p70S6Ki described above. To this end, we performed a transferrin uptake assay in HeLa KO μ2 cells transfected with plasmids encoding myc-μ2^{WT} or myc-μ2^{S45A}, a μ2 variant in which S45 has been replaced by alanine so that the protein cannot be phosphorylated at this site. Myc-μ2^{WT} and myc-μ2^{S45A} were expressed at comparable levels and had no effect on the expression levels of endogenous β2 AP2 subunit and TrfR (**Fig. 4A, B**). Comparison of these lines showed that the uptake of fluorescently labeled transferrin was significantly decreased in μ2^{S45A} cells compared with μ2^{WT} cells (**Fig. 4C, D**). However, this difference was not due to a reduced

amount of TrfR (**Fig. 4E, F**) or downregulation of TrfR surface expression reflected by the surface binding of transferrin (**Fig. 4G, H**). These results indicate that the absence of S45-μ2 phosphorylation, just like p70S6K inhibition, significantly downregulates CME.

Substitution of serine 45 to alanine leads to apm-2 loss-of-function-like phenotypes in C. elegans.

Our previous results have shown that phosphorylation of S45-μ2 is essential for transferrin uptake. Yet, its relevance to AP2 functions *in vivo* remains undetermined. *C. elegans* has emerged as a valuable model for exploring AP2 functionality and early CME processes. Worms with loss-of-function alleles of *apm-2* (also referred to as dpy-23; WormBase ID: WBGene00001082), which encodes the μ2 homolog, display three primary phenotypes: (i) variable dumpy phenotype (Dpy), (ii) defect in egg laying, and (iii) slightly uncoordinated phenotype (Unc) [31–33].

The serine 45 of μ2 is conserved in humans and *C. elegans* (**Fig. S2A**). Prompted by this, we assessed the *in vivo* ramifications of blocking S45 phosphorylation in relation to the phenotypes observed in loss of function *apm-2* alleles, using the CRISPR-Cas9 technique to generate worms with S45 replaced by alanine (**Fig. S2B**), analogous to the experiments conducted in HeLa cells. *Dpy* mutants are characterized by a thicker midbody and shorter length [34]. Therefore, we measured the size of *apm-2* (S45A) mutant worms. At the adult stage (day 2), the body width and length of these worms were different from control counterparts (**Fig. 5A-C**), reflecting the characteristics of the *Dpy* phenotype, including a reduced head size (**Fig. 5A**) [35]. Given the observed egg-laying defect associated with the loss of *apm-2* [31], we investigated the egg-laying behavior of the APM-2 (S45A) producing worms. Our results showed that these animals laid significantly fewer eggs than their wild-type counterparts (**Fig. 5D**), yet there was no difference in offspring survival (**Fig. S2C**) or longevity (**Fig. S2D**).

Finally, we analyzed several locomotory parameters of young adult *apm-2* (S45A) mutants. While these worms and their wild-type counterparts were largely similar in most of the assessed parameters, we observed statistically significant differences in the *apm-2* (S45A) animals, particularly in backward movement - evidenced by the reduced number of reversals, cumulative reversal time, and the amplitude of their sinusoidal movement (**Fig. 5E-G**). Overall, we conclude that the absence of S45-μ2 phosphorylation in worms mimics, although with lower robustness, phenotypes previously described for *apm-2* null mutants, confirming the physiological significance of this particular posttranslational μ2 modification.

Phosphorylation of S45 of μ2 influences the conformational changes of AP2 and is needed for the effective CME.

Based on our results, p70S6K-dependent phosphorylation of S45 of μ2 is needed for efficient CME. At the same time, S45 phosphorylation seems to be unrelated to the ability of μ2 to be effectively incorporated into AP2 or its interaction with TrfR. Therefore, based on available literature concerning AP2 conformational changes [1,2,4–7,36], we hypothesized that p70S6K-dependent phosphorylation od S45-μ2 might influence the conformational changes of the AP2 complex and thus the dynamics needed for efficient CME process. To verify whether phosphorylation of S45 would favor one of the AP2 conformations we probed for conformational changes using the proximity ligation assay (PLA) between myc-tagged μ2 subunit with either TrfR or AP2 β2 subunit. According to our analysis of available structural data [1,2,7] in case of a fully open AP2 complex facing the cell membrane (i.e. open +) the myc-tag, which is placed in the linker region between the N- and C-terminal subdomains in position S238-G250 aa of μ2 [30], should be trapped between the membrane and the rest of the complex and not easily accessible for antibodies (**Fig. S3A)**. On the other hand, in closed AP2 conformation antibodies against myc-tag

should easily recognize the epitope. Thus, we assumed that in the case of open+ conformation the PLA signal between myc-μ2 and TrfR or β2 should be greatly reduced. Indeed, in HeLa KO μ2 cells transfected with myc-$\mu2^{WT}$, serum-starved and treated with p70S6Ki, the number of fluorescent myc-TrfR or myc-β2 PLA objects was significantly lower, compared with the control variant (**Fig. S3B-E**). We also performed PLA to analyze the interaction between TrfR or β2 and overexpressed myc-$\mu2^{WT}$ or myc-$\mu2^{S45A}$. We observed that the number of myc-TrfR or myc-β2 PLA objects was significantly lower in the $\mu2^{S45A}$ variant compared with $\mu2^{WT}$ (**Fig. S3F-I**). Altogether these results suggest that p70S6K-dependent phosphorylation of S45 is important for the AP2 complex conformational changes and lack of S45 phosphorylation probably favors an open, membrane-bound AP2 complex, likely at the expense of closed cytoplasmic one, leading to inefficient CCP formation and CME cargo internalization.

If the substitution of μ2 S45 to alanine alters the conformational transitions of the AP2 complex, it should affect the dynamics of CCPs formation. To verify this assumption, we turned to the TIRF method. We constructed HeLa KO μ2 cell lines stably expressing $\mu2^{WT}$ or $\mu2^{S45A}$ together with EGFP-CLCa. Both cell lines had comparable expression levels of endogenous AP2 α and β2 subunits as well as exogenous myc-μ2 and EGFP-CLCa. The immunoprecipitation experiments showed that both $\mu2^{WT}$ and $\mu2^{S45A}$ were incorporated effectively into endogenous AP2 in these lines and their binding to β2 and α adaptins was similar (**Fig. 6A, B, Fig. S4**). Thus, as in the case of data obtained with p70S6K inhibitor, we did not observe major differences between cells stably expressing $\mu2^{WT}$ or $\mu2^{S45A}$ in AP2 subunits expression and interaction. Considering these results, we decided to check if p70S6K-dependent μ2 S45 phosphorylation might influence the efficiency and dynamics of CCP formation, which could explain the observed decrease in TrfR and PDGFR internalization seen upon p70S6Ki treatment. Thus, we compared the dynamics of

CCP formation in the HeLa μ2 KO cell lines stably expressing $\mu2^{WT}$ or $\mu2^{S45A}$ together with EGFP-CLCa. In cells expressing $\mu2^{S45A}$, we observed more CSs not incorporated into endocytic vesicles and fewer CCPs than in the $\mu2^{WT}$ variant (**Fig. 6C**). We also observed that the matured CCPs were smaller and that the rate of clathrin polymerization was slightly reduced in 40-60 s cohort of CCPs in $\mu2^{S45A}$ cells (**Fig. 6D**), which together with an increased number of clathrin structures can be a result of disturbed CCP nucleation. At the same time in cells expressing $\mu2^{S45A}$ we observed an increased fraction of CCPs living above 40 s (**Fig. 6E, F**). Under physiological conditions, on average 30- 40 seconds after the onset of CME, clathrin-coated vesicles are disassembled and their cargo is shifted to early endosomes [37,38]. Thus, our TIRF data showing more long-lived CCPs in $\mu2^{S45A}$ cells point to the scenario where the inability to phosphorylate μ2 leads to an overall disruption of CME, potentially caused by disturbed dynamics in AP2 conformational stages cycle.

Finally, the results obtained with TIRF pointed to less efficient CCP formation in cells in which μ2 could not be phosphorylated in a p70S6K-dependent manner. To further verify this observation, cells expressing $\mu2^{WT}$ and $\mu2^{S45A}$ were compared for the number and ultrastructure of CCPs and CCVs using electron microscopy. The parental line - HeLa KO μ2 - served as a negative control with diminished AP2 function. Indeed, significantly fewer CCPs/CCVs were observed in the KO μ2 cells and the cells with exogenous $\mu2^{S45A}$ expression compared to the $\mu2^{WT}$-expressing cells (**Fig. 6G, H**). In summary, we conclude that p70S6K-dependent phosphorylation of μ2 at S45 is vital for proper function of the AP2 complex and efficient formation of CCPs and, in consequence, for CME in mammalian cells (**Fig. 7**).

Discussion

The role of post-translational modifications of the AP2 μ2 subunit in the regulation of CME is still not fully understood. To date, most of the studies focused on the phosphorylation at T156 [7,10–

12], while the importance of other μ2 modifications, e.g., phosphorylation of S45, and their molecular consequences remain elusive. In this work, we have reported that p70S6K positively regulates CME by indirectly controlling the phosphorylation of S45-μ2. Loss of this post-translational modification results in impaired dynamics of CCP formation and decreased CME in cells cultured *in vitro* and leads to a phenotype resembling the loss of function of the AP2 complex in *C. elegans*. Our results suggest that S45-μ2 phosphorylation is important for the regulation of conformational changes of the AP2 complex. Lack of this phosphorylation ultimately leads to reduced efficacy of CME, which might be caused by favoring the membrane-bound AP2 conformation.

p70S6K is essential for effective CME.

Several kinases have been shown to regulate CME by phosphorylating either the CME cargo or the elements of the endocytic machinery [9], but the contribution of p70S6K to CME has not been studied in depth. Our study shows that p70S6K activity is essential for endocytosis of TrfR and PDGFR in human cells. MS analysis revealed that one threonine and three μ2 serines, including S45, were phosphorylated in a p70S6K-dependent manner. However, the results of *in vitro* kinase assays do not support that μ2 is a direct target of p70S6K (Fig. 3). These observations are consistent with the predictions of various bioinformatic tools (e.g., Kinexus, GPS5, NetPhos 3.1), which do not list p70S6K as a potential kinase for S45-μ2. Although we cannot exclude the possibility that some essential co-factors allowing the phosphorylation of this particular target were missing in our assays, this observation raises questions about the mechanism explaining the impact of p70S6K activity on this phosphorylation. So far, the only kinase shown to phosphorylate μ2 at S45 was CDK5 immunoprecipitated from murine brain [13]. Thus, p70S6K could potentially control the CDK5 activity. However, all available data suggest that p70S6K is a CDK5 substrate

rather than its upstream kinase [39,40]. Moreover, bioinformatic predictions point to JNK1-3, ERK1, ERK2, ERK5 and p38 as top candidates for S45-μ2 kinase. However, JNKs, p38 and ERKs directly or indirectly control p70S6K and not vice versa [41–45]. Finally, p70S6K might protect μ2 from being dephosphorylated by phosphatases. p70S6K has been shown to phosphorylate PP1α in PC3 cells, leading to its inactivation [46]. Nevertheless, PP1α plays a promoting role during CME [47], ruling out that it is a part of the discussed mechanism. Although our results clearly show that CME and S45-μ2 phosphorylation are controlled by p70S6K, further studies are needed to identify the exact mechanism. In addition to the possibilities discussed above, it cannot be excluded that the specific spatial organization of the AP2 complex and p70S6K at the plasma membrane is needed for the phosphorylation to occur, which could not be mimicked in our cell-free system using recombinant proteins. In this context, it is worth mentioning that p70S6K translocates to the plasma membrane upon stimulation with PDGF, substantiating the notion that its specific subcellular localization might be key for the activity towards particular substrates [48].

The role of S45-μ2 phosphorylation in regulating CME.

We found that S45-μ2 is phosphorylated in a p70S6K-dependent manner and that this modification is essential for efficient TrfR internalization. This result appears to contrast with the conclusions of Liu et al. (2019) [13] who showed that the presence of a short peptide competing with S45 phosphorylation enhances the internalization of EGFP-TRPV1 overexpressed in HEK cells. The reason for this difference is not entirely clear, but in our opinion, there are at least two possible explanations. First, the different cargo studied; second, the alternative approaches to inhibit S45 phosphorylation. In their work, Liu et al. (2019) analyzed the overexpressed TRPV1 receptor levels in subcellular fractions, while endogenous TrfR levels were shown as a gel loading control and appeared unchanged regardless of the manipulations applied to remove CDK5 or interfere

with S45 phosphorylation. Thus, in the study by Liu et al. (2019), the internalization of EGFP-TRPV1 and endogenous TrfR appear to be differentially affected by the absence of CDK5 or diminished S45-μ2 phosphorylation. Of note, Liu et al. (2019) used an indirect approach to prevent S45-μ2 phosphorylation: the "decoy" peptide - tat S45 as a competitor for endogenous S45-μ2. Therefore, the inhibition achieved was probably acute, and the endogenous protein could still be phosphorylated, albeit to a much lesser extent. In our approach, the wild-type μ2 was replaced by the phospho-deficient variant, so the lack of μ2 phosphorylation was chronic and irreversible. Since the lack of S45 phosphorylation likely affects the preference of AP2 to remain in one of the conformations, the acute and long-term effects are presumably different. Therefore, given the significant differences in the design of the two studies, these results could be seen as complementary, jointly supporting the role of S45 phosphorylation in the regulation of CME.

Lack of S45-μ2 phosphorylation potentially stabilizes the membrane-bound AP2.

So, what could be the function of S45-μ2 phosphorylation, and how the CME defects observed in cells expressing a non-phosphorylable mutant instead of the wild-type μ2 can be explained in this context? Based on our observations, we hypothesize that the S45-μ2 phosphorylation/dephosphorylation cycle may have a function in the conformational changes of AP2 by stabilizing the steps of the cycle. During the CME, AP2 is recruited from the cytoplasm, adopts an open (active) conformation and binds cargo, allowing clathrin coat attachment and subsequent CCV formation and cargo internalization. After CCV formation, AP2 dissociates from the CCV and transitions to a closed (inactive) conformation. Altogether, it is known that a sequential hierarchy of interactions controls AP2 activation, coordinating the early phases of CCP formation and stabilization [3]. The T156 phosphorylation/dephosphorylation cycle of μ2 is essential for the conformational changes of AP2 and cargo binding. Blocking of AP2 in either of

its conformations results in decreased CME efficiency. The S45 phosphorylation/dephosphorylation cycle of μ2 may also contribute to the conformational changes of AP2. However, in contrast to T156 phosphorylation, it would stabilize particular conformational states instead of actively influencing the transitions between them. An open, membrane-bound state would characterize AP2 with non-phosphorylated S45, whereas phosphorylated μ2 could be characteristic of a closed AP2. Through quantitative analysis in living cells (TIRF microscopy), we were able to measure the distinct early stages of CME. The prolonged duration of CCPs observed in our live cell imaging indeed points to the stabilization of the open form of AP2 at the cell membrane in the case of the μ2 S45A variant (Fig. 6). At the same time, if the S45A mutant is present in the cell, this stabilization would lead to a gradual depletion of cytoplasmic AP2. The combination of these two phenomena should lead to the decrease in the internalization of TrfR or PDGFR that we observed (Fig. 2 and 4), as well as a lower number of efficiently formed CCPs and CCVs (Fig. 6). To sum up, our results suggest that an uninterrupted cycle of S45-μ2 phosphorylation/dephosphorylation is indispensable for AP2 conformational changes and essential for the proper progression of CME in mammalian cells.

mTOR-p70S6K-AP2 axis might contribute to coupling of CME to the metabolic status of the cell.

Given that p70S6K-dependent phosphorylation of S45-μ2 regulates early steps of CME, the question arises regarding the potential (patho)physiological significance of this mechanism. Since mTOR-p70S6K pathway is one of the key sensors of the metabolic status of the cell, it is tempting to speculate that the mTOR-p70S6K-AP2 axis may contribute to the coupling of CME with the current metabolic needs. Such dynamically regulated coupling is key for maintaining homeostasis and safeguarding proper cell growth, migration, and cell divisions, among others [49,50]. Thus,

the positive influence of the mTOR-p70S6K pathway on the initiation of CCV formation could serve to adjust the endocytosis rate to the current status of the cell.

On the other hand, the very same mechanism could also be implicated in the pathological conditions linked to mTOR and p70S6K overactivation, such as mTORopathies [14,15] and cancer [45,51]. Contribution of dysregulated endocytosis to cancer pathogenesis is becoming increasingly recognized. Nutrient intake, signaling from cell membrane receptors, and the turnover of adhesion molecules exemplify key cellular processes that highly depend on the CME [50,52–54] and are at the same time crucial for oncogenesis. Thus, it has been proposed that increased metabolic demands, invasiveness, and rapid division of cancer cells are supported by dysregulated endocytic pathways [55–57], and that CME can represent a target in cancer therapy [58]. Based on our data, CME may be a potential therapeutic target not only in cancer but also in mTORopathies. The presumed involvement of dysregulated CME in supporting cell hypertrophy in these diseases is an exciting hypothesis for future studies.

Material and Methods

Antibodies

Commercially available primary antibodies used for this study are listed in Table 1.

Table 1. Primary antibodies used for the study

Primary antibody	Manufacturer, catalog	Application, dilution
Mouse anti-μ2	BD Bioscience #611350	WB 1:250 IF 1:200
Rabbit anti- PDGFRβ	Santa Cruz #432	WB 1:1000 IF 1:200

Mouse anti-EEA1	BD #610457	IF 1:400
Rabbit anti-β2	Thermo Fisher #PA1-1066	PLA 1:100 WB 1:500
Mouse anti-β2	Santa Cruz #74423	WB 1:500
Mouse anti-α1/2	BD #610502	WB 1:500
Mouse anti-S6	Cell Signaling #2217	WB 1:1000
Rabbit anti-P-S6 S235/236	Cell Signaling #4858	WB 1:1000 IF 1:200
Mouse anti-myc-tag	Cell Signaling #2276	PLA 1:200 IF 1:200 WB 1:500
Rabbit anti-myc-tag	Cell Signaling #2272	PLA 1:200 IF 1:200 WB 1:500
Mouse anti-tubulin	Sigma-Aldrich #T5168	WB 1:5000
Rabbit anti-tubulin	Abcam #ab4074	WB 1:3000
Mouse anti-GAPDH	Millipore #MAB374	WB 1:1000
Mouse anti-TrfR	Invitrogen #13-68000	PLA 1:100 IF 1:100
Mouse anti-TrfR	Santa Cruz #32272	WB 1:500
Rabbit anti-hamartin	Cell Signaling #6935S	WB 1:1000
Rabbit anti-GFP	MBL #598	WB 1:1000

PLA – proximity ligation assay; WB- western blotting; IF – immunofluorescence

Alexa Fluor 488-, 568-, and 647-conjugated secondary antibodies (anti-mouse, and anti-rabbit) were obtained from Thermo Fisher. Horseradish peroxidase-conjugated secondary antibodies were

obtained from Jackson ImmunoResearch. Anti-mouse/anti-rabbit IRDye® 680RD and IRDye® 800CW were from LI-COR Biosciences.

Plasmids

The following plasmids were obtained from other researchers or are commercially available: pCDH-EF1a-MCS-PGK-PURO, pVSV-G, pRSV-Rev and pCgpV plasmids (Cell Biolabs, Inc., SBI's lentiviral system; kind gift from Krystyna Bienkowska-Szewczyk lab), pUltra-Hot (Addgene #24130), pUltra-Chili (Addgene, # #48687), HA-BirA [59] (kind gift from Casper Hoogenraad lab), pEGFPC2-Avi-tag-βGal [60], pIRESneo2-myc-Ap2m1 [30] (kind gift from Robinson lab); p70S6K^{WT}, p70S6K^{K100R}, His-RPS6 (all kind gift from Ivan Gout), pGEX-4T1 (Merck, catalog no. GE28-9545-49), pMD (Addgene: 12259; kind gift from Malcolm Moore), pPAX (Addgene: 12260; kind gift from Malcolm Moore), pGFP-CLCa (kind gift from Lucas Pelkmans), pLKO.1-TRC-shTSC1 [61]. The pIRESneo2-myc-Ap2m1^{S45A} was obtained by site-directed mutagenesis of pIRESneo2-myc-Ap2m1 with use of QuikChange Site-Directed Mutagenesis System (Stratagene, Santa Clara, CA) and following primers: Ap2m1S45A_fw (5'-CGGCAGCAGGTGCGCGCCCCTGTCACAAACATCGC-3') and Ap2m1S45A_rv (5'-GCGATGTTTGTGACAGGGGCGCGCACCTGCTGCCG-3'). pUltra-Hot-μ2^{WT} and μ2^{S45A} plasmids for lentiviral vectors construction were obtained by PCR amplification of μ2^{WT} and μ2^{S45A} encoding sequences from pIRESneo2-myc-Ap2m1^{WT} and Ap2m1^{S45A} plasmids, respectively, using forward 5' AAAATCTAGAACCGGTATGATCGGAGGCTTATT 3' and reverse 5' AAAAGCTAGCCTAGCAGCGGGTTTCGTAAATG 3' primers and subsequent subcloning into XbaI and NheI sites of pUltra-Hot plasmid. To construct pGEX4-μ2$^{WT(aa1-156)}$ and μ2$^{S45A(aa1-156)}$ first 468 nucleotides (corresponding to the first 156 aa of μ2, either WT or S45A) were ordered as synthetic double stranded GeneArt strings (Thermo Fisher Scientific). μ2

sequences were flanked with sequences which allowed cloning the DNA fragments into pGEX4T-1 BamHI/SalI restriction sites using sequence and ligase independent cloning method (SLIC, [62]) (5' GATCTGGTTCCGCGTGGATCC' and 5' GTCGACTCGAGCGGCCGCATC 3', respectively). To generate plasmid to produce lentiviral vectors encoding clathrin light chain (CLCa) in N-terminal fusion with GFP (pCDH-EF1a-MCS-PGK-PURO-GFP-CLCa), pGFP-CLCa was used as a template for PCR reaction. The reaction was performed with Q5® High-Fidelity DNA Polymerase (New England BioLabs Inc.) with following primers: forward 5' AAAAGCGGCCGCGCCACCATGGTGAGCAAGG 3' and reverse 5' AAAAGTCGACTCAGTGCACCAGGGGGGCCT 3'. PCR product was subcloned into EcoRI and SalI restriction sites of pCDH-EF1a-MCS-PGK-PURO. BioGFP-p70S6K^{WT}, BioGFP-p70S6K^{K100R} (kinase dead) were obtained by subcloning PCR amplified p70S6K^{WT} and p70S6K^{K100R} sequences into EcoRI/SalI sites of A698 plasmid (pEGFPC2-Avi-tag). The following primers were used: forward 5' GAAGAATTCATGGAGGCAGGAGTGTTTGACATAG 3' and reverse 5' GTCGTCGACTCATAGATTCATACGCAGGTGC 3'. pUltra-mCherry-shTSC1 plasmid was generated by digestion of pSuper-GFP shTSC1 vector with PstI and SalI restriction enzymes. Next, the fragment encoding the H1 promoter and TSC1 shRNA coding sequence (GAAGAAGCTGCAATATCTA) was blunted and cloned into the pUltra-mCherry vector at the SnaBi site. The TdTomato coding sequence in the vector was replaced with mCherry derived from pUltra-Hot plasmid, using SpeI/BsrGI restriction enzymes. Super-GFP shTSC1 vector was generated by annealing oligonucleotides: forward 5' GATCCCCGAAGAAGCTGCAATATCTATTCAAGAGATAGATATTGCAGCTTCTTCTTT TTGGAAA 3' and reverse 5'

AGCTTTTCCAAAAAGAAGAAGCTGCAATATCTATCTCTTGAATAGATATTGCAGCTT CTTCGGG 3', followed by cloning into BglII/HindIII restriction sites of pSuper GFP.

pEGFPC2-Avi-tag-Ap2m1 was obtained by subcloning PCR amplified Ap2m1-pCDNA sequences into BglII/HIndIII sites of A698 plasmid (pEGFPC2-Avi-tag). The following primers were used: forward 5' AGAAGATCTCTATGATCGGAGGCTTATTCATC 3' and reserved 5' AAGAAGCTTCTAGCAGCGGGTTTCGTAAATGCC 3'.

Generation of lentiviral vectors and cell lines

Lentiviruses were generated by transfection of HEK293T cells with calcium phosphate method (CalPhos™ Mammalian Transfection Kit, Takara) for 48 hours. After this time supernatants were collected and used for transduction of HeLa cells wild type or HeLa KO μ2. First, we generated and sorted cell lines expressing EGFP-CLCa, following transduction with lentiviruses carrying μ2 constructs or TSC1 shRNA. All generated cell lines were sorted for the same level of EGFP and mCherry fluorescence between variants using BD FACSAria II cell sorter (Becton Dickinson) using blue laser (488 nm, 13 mW) and 530/30 and 616/23 nm emission filters.

C. elegans *strains*

Worms were maintained on nematode growth medium (NGM) plates seeded with OP50 *Escherichia coli* bacteria at 20°C unless otherwise stated [63]. The amp-2 gene mutant (c. 375 T>C. p.S45A) was generated using CRISPR/Cas9 method as previously described by Dokshin et al. [64]. The crRNA sequence used was TCGCTCGCCAGTCACCAACA. The apm-2 gene locus was sequenced, and mutation confirmed. The resulting amp-2(WOP370) was backcrossed to wild-type N2 worms.

Drugs treatment

p70S6K inhibitor (Calbiochem, PF-4708671) was used in 10 μM concentration. p70S6Ki was dissolved in DMSO (Sigma-Aldrich, D8418), whose final concentration in the culture medium did not exceed 0.1%.

Cell line cultures and transfection

HeLa cells and HeLa KO μ2 cells were a kind gift from Juan Bonifacino laboratory. HEK293T cells and CCD-1070Sk (CRL-2091) human normal foreskin fibroblasts were purchased from ATCC. HEK293T and HeLa cells were grown in Dulbecco's modified Eagle's medium (DMEM) that contained 10% fetal bovine serum and 1% penicillin-streptomycin (all from Sigma-Aldrich). CCD-1070Sk cells were cultured in Minimum Essential Medium (MEM) supplemented with 10% fetal bovine serum (FBS), and 2 mM L-glutamine (all from Sigma-Aldrich). All cells were maintained at 37°C in a 5% CO_2 atmosphere and PCR-based tests for mycoplasma contamination were routinely performed. For experiments with use of confocal or TIRF microcopy, cells were grown on precision cover glasses (Marienfeld, 0107032). HEK293T and HeLa cells at 70% confluency were transfected using polyethylenimine PEI 25K™ (Polysciences, 23966) according to the manufacturer's protocols. After transfection cells were grown in DMEM supplemented with 5% FBS for 48 h.

PLA

Fixed cells were incubated with a pair of primary antibodies, raised in two different species (rabbit anti-myc and mouse anti-β2 or anti-TrfR) diluted in PBS containing 0.2% Triton-X100, and 1% donkey serum at 4°C overnight. The coverslips were washed twice for 5 min in antibody buffer provided by PLA kit manufacturer (Sigma-Aldrich, DUO92101) and then the PLA reaction was performed with the usage of DUO LINK PLA probes anti-mouse minus (Sigma-Aldrich,

DUO92004) and anti-rabbit plus (Sigma Aldrich, DUO92002) diluted in antibody diluent. Next the coverslips were washed two times for 5 min with buffer A (Sigma-Aldrich, DUO82046). The ligation and amplification were performed according to the manufacturer's protocol with the use of DUO LINK In Situ Detection Reagents Red (Sigma-Aldrich, DUO92008). After PLA reaction coverslips were washed 2 times with buffer B (Sigma-Aldrich, DUO82048) and incubated 10 min with Alexa 488-conjugated Phalloidin diluted in buffer B. After incubation cells were washed two times with buffer B. Finally, cells were mounted with DUO LINK in situ mounting medium containing DAPI (Sigma-Aldrich, DUO82040). For each experiment, negative controls without primary antibodies were prepared.

Immunofluorescence

HeLa KO μ2 cells were fixed with 4% PFA (containing 4% sucrose in PBS pH 7.4) for 10 min and washed three times with PBS. After fixation cells were blocked for 1 hour in PBS containing 5% donkey serum and 0.3% Triton X-100. Primary antibodies were incubated in PBS containing 1% BSA and 0.3% Triton X-100 at 4°C overnight. After overnight incubation coverslips were washed three times with PBS. Alexa 488- and Alexa 594–conjugated secondary antibodies were used for 1 hour at room temperature. Coverslips were washed three times with PBS and mounted with Prolong Gold with DAPI (Thermo Fisher, P36941).

Transferrin uptake and PDGFR internalization assay

Cells were starved at 37°C in a 5% CO2 atmosphere in non-supplemented DMEM medium for 18 h. Alexa Fluor 647-conjugated transferrin from human serum (Thermo Fisher, T23366) was then added to the cells for 5 min at a final concentration of 25 μg/ml. The cells were then rinsed with medium, fixed with 4% paraformaldehyde (containing sucrose), and washed 3 times with PBS. PDGFR internalization by CCD fibroblasts and results quantification were performed as described

in Jastrzebski et al. (2017) [28]. In brief cells were treated with PDGF (PeproTech #100-14B; 50 ng/ml) for 15 minutes and fixed with 4% paraformaldehyde.

For transferrin surface staining HeLa KO μ2 cells after starvation for 18 h were incubated for 15 min on ice following 15 min incubation on ice with transferrin conjugated with Alexa Fluor 647 (25 μg/ml) in DMEM without FBS. Next cells were washed with cold PBS and fixed with cold 4% paraformaldehyde for 15 min on ice and 15 min at room temperature, followed by washing 3 times in PBS.

Fixed cells image acquisition and analysis

Images of fluorescently labeled *in vitro* cultured cells were acquired with a Zeiss LSM800 confocal microscope (40× or 63× objective) with the settings kept constant for all scans in a series. Z-stacks (interval 0.2 μm – 0.5 μm) were converted to single images using a maximum intensity projection. The mean fluorescence intensity was measured using *ImageJ,* except for PDGFR internalization analysis that was performed as described previously [28]. The number of PLA objects per cell was counted in *ImageJ* software using the "Analyze Particles" plugin. The average number of PLA objects per cell was then calculated for each condition, and the results were normalized by subtracting the average number of PLA objects per cell calculated for the negative control. The obtained average number of PLA objects per cell was further normalized by dividing the obtained values from a particular experiment by the average number of PLA objects per cell from the control variant from at least three repetitions.

TIRF microscopy

Cells ($3x10^5$) were seeded on coverslips coated with matrigel 2-3 hours before imaging. The cells were imaged on the Andor Revolutions XD imaging platform equipped with Zeiss TIRF illuminator, Chroma dual band 488/561 TIRF filter set, Zeiss 100x/1.46 Plan-Apo objective,

Optovar magnification changer set at 1.6x and LucaR EM-CCD camera (Andor). Time-lapses were acquired using IQ3 software (Andor) at 1 Hz for 5 minutes. Detection and lifetime analysis of clathrin structures was performed with the cmeAnalysis software [25] according to the software manual. Descriptive statistics of populations (1 n = 1 movie that typically contained 1-3 cells in the field of view) were shown as box plots (boxes indicate the quartiles and whiskers extend to extreme data points). Significance of differences between populations was tested with the ranksum test (Matlab).

Electron Microscopy sample preparation, processing and imaging

Electron microscopy was performed as described earlier [65]. Briefly, cells were grown on coverslips (Thermanox plastic coverslips; NUNC Brand Product) on 24-well plate. 3 h after seeding, cells were fixed in 2.5% glutaraldehyde for 2 hours, followed by 3 washings with PBS. The material was then postfixed with 1% osmium tetroxide for 1 h, washed with water, and stained in 1% aqueous uranyl acetate overnight at 4°C. In the next step, cells were dehydrated with increasing concentrations of ethanol and embedded with epoxy resin (Sigma Aldrich, #45-359-1EA-F). Resin-infiltrated samples were then incubated at 60ºC for 72 h for polymerization. Polymerized blocks with cells were trimmed and cut with a Leica ultramicrotome (EM UC7) for ultrathin sections (65 nm thick). Sections were placed on nickel grids, mesh 200 (Agar Scientific, AGG2200N). The material was examined with a transmission electron microscope Tecnai T12 BioTwin (FEI, Hillsboro, OR, USA) equipped with a 16-megapixel TemCam-F416 (R) camera (TVIPS GmbH).

Electron Microscopy images quantification

Images of the cells captured at 13.000 x magnification were assembled to have continuous cytosol ultrastructure. CCPs, visualized with electron microscopy, were manually recognized and counted.

The area of the cell was analyzed in *ImageJ*, from micrographs of lower magnification (2.900), allowing to fit the whole cell on one or two pictures. Obtained values were then collected and analyzed in Excel software.

Whole-cell lysate preparation

For Western blot analysis of proteins in whole cell lysate, cells were lysed in the lysis buffer (20 mM Tris pH 7,5; 150 mM NaCl; 2 mM EDTA; 0.5% Triton X-100; 0.5% NP-40; 2 mM $MgCl_2$; 10% glycerol; protease and phosphatase inhibitors). For total protein concentration in whole-cell lysates, Pierce BCA Protein Assay Kit (Thermo Fisher, 23225) was used according to the manufacturer's instructions. Then 4x Laemmli sample buffer was added to lysates followed by boiling for 5 min at 95°C.

Production and purification of recombinant proteins in bacteria

Recombinant proteins were produced in *E. coli* BL21 strain. Individual clones transformed with plasmids encoding proteins of interest were picked from the plates and inoculated to 5 ml of LB with an appropriate antibiotic. After overnight cultivation at 37°C with shaking, bacteria were refreshed with a new medium in 1:20 ratio, and further cultured until reaching OD_{600} = 0.4 - 0.6. Protein production was induced using 1 mM Isopropyl β-d-1-thiogalactopyranoside (IPTG; ROTH, CN08.3). Recombinant proteins were produced at 30°C for 3 h. Next, cultures were centrifuged at 4,500 x *g* for 10 min. The pellet of bacteria with GST-tagged proteins was resuspended in a lysis buffer consists of 50 mM Tris (pH, 8.0), 150 mM NaCl, 0.1% Triton X-100, protease inhibitors, while the pellet of bacteria with His-tagged proteins were resuspended in lysis buffer consists of 50 mM $NaH_2PO_4/Na_2H_2PO_4$ (pH 8.0), 300 mM NaCl, 10 mM imidazole, 10% glycerol, 10 mM β-mercaptoethanol, 0.1% Triton X-100, 1 mM PMSF. After resuspension, cells

were lysed on ice by sonication with Sonics VCX130 PB sonicator (Vibra-Cell) in two sessions of 25 sec. with 70% amplitude. After sonication, lysates were centrifuged at 13,000 x *g* for 5 min.

Supernatant of His-tagged proteins was added to HIS-Select Nickel Affinity Gel (Sigma Aldrich, P6611) in ratio 40 µl beads, for each 1 ml of original bacterial culture and incubated for 1 h with end-to-end rotation at 4°C. Next beads were washed three times: first with lysis buffer, second with lysis buffer contained 2 M NaCl and third with lysis buffer with 20 mM imidazole. After each wash beads were centrifuged at 5000 x *g* for 30 sec. Finally, His-tagged proteins were eluted with elution buffer (50 mM $NaH_2PO_4/Na_2H_2PO_4$ (pH 8.0), 300 mM NaCl, 250 mM imidazole, 10% glycerol, 10 mM β-mercaptoethanol, 0.1% Triton X-100, 1 mM PMSF). Supernatant of GST-tagged proteins was added to Glutathione-Sepharose 4B resin (Merck, GE17-0756-01) in ratio 40 µl beads, for each 1 ml of original bacterial culture and incubated for 1 h with end-to-end rotation at 4°C. Next beads were washed three times with cold PBS. After each wash beads were centrifuged at 5000 x *g* for 30 sec. After the last wash volume was adjusted to 1 ml with PBS. The resin with GST-tagged proteins was then used for kinase assays.

Kinase assays

In vitro phosphorylation assay was performed for 20 min at 30°C in a kinase assay reaction buffer (50 mM MOPS pH 7,4; 12 mM MgCl2, 2 mM EGTA, 1 mM DTT) in presence of 2,5 µCi [γ-^{33}P]ATP (Hartmann Analytic GmbH, Braunschweig, Germany) and 2.5 mM "cold" ATP using recombinant, active p70S6 kinase (Biovision, 7725) or biotinylated p70S6KBioGFP WT and p70S6KBioGFP kinase dead (KD) (obtained as described in *Avi-tag pull down of in vivo biotinylated proteins* section) and fragments (aa 1-156) of recombinant proteins $\mu2^{WT}$ or $\mu2^{S45A}$, or RPS6 his tag (as positive control) or GST (as negative control) as substrates. The reaction was stopped by adding 4x Laemmli sample buffer and boiling for 5 min at 95°C. Next, samples were

separated by SDS-PAGE. The gel was stained with Coomassie Brilliant Blue and dried. The radioactive signal was detected and analyzed using a Typhoon Trio+ Phosphorimager (GE Healthcare).

Cell surface biotynylation assays

The assay was performed according to the manufacturer's protocol Pierce Cell Surface Biotinylation and Isolation Kit (Thermo Fisher, A44390).

Avi-tag pull down of in vivo biotinylated proteins

HEK293T cells co-expressing BirA together with Avi-tag proteins were harvested and lysed on ice in lysis buffer for 15 min. M-280 streptavidin Dynabeads (Thermo Fisher, 11205D) were washed with lysis buffer (20 mM HEPES, pH 7.5, 120 mM KCl, 0.3% CHAPS supplemented with protease and phosphatase inhibitors). The cell lysate was added to the previously prepared M-280 streptavidin Dynabeads and incubated together for 1 h at 4°C while rotating. Then, beads were washed on ice four times in washing buffer (20 mM HEPES, pH 7.5, 500 mM KCl, 0.1% CHAPS). The samples were used for kinase assays or denatured in 2x Laemmli sample buffer and analyzed via SDS–PAGE followed by silver staining.

MS/MS Analysis of Protein Phosphorylation

To identify phosphorylated residues within the μ2 sequence, GFP-Avi-tag-μ2 was overexpressed in HEK293T cells, purified as described above, denatured, and subjected to SDS-PAGE. The gel was stained with silver, and bands that corresponded to μ2 were excised. The samples were then subjected to "in-gel digestion" and obtained peptides were analyzed by mass spectrometry as described previously [66], but without an enrichment step.

Western blotting

Protein samples were analyzed by SDS–PAGE electrophoresis and immunoblotting according to standard laboratory protocols. Primary antibodies used for Western blotting are listed in Table 1. For protein separation, 10% polyacrylamide gels were run at 90 V for about 20 min and then 120 V until the loading buffer reached the bottom of the gel. Proteins were transferred to a nitrocellulose membrane (Amersham™ Protran, Sigma GE10600002) using a wet blot transfer system (Bio-Rad Laboratories) for 90 min at 100 mA. Membranes were blocked for 1 h with 5% nonfat milk in TBS-T (tris-buffered saline with 0.05% Tween 20). Primary antibodies were incubated overnight at 4°C. After washing three times with TBS-T , the secondary antibody (1:10000 in 5% TBST-milk, Jackson ImmunoResearch) was incubated for 1 hour at room temperature. The signals were detected using ECL solution or ImageStudioLite (LI-COR). In case of fluorescent signal detection in LI-COR system, TBS was used in all steps instead of TBS-T.

Immunoprecipitation

For the immunoprecipitation (IP) of μ2 with myc tag from HeLa KO μ2, cells stably expressing EGFP-CLCa and myc-$\mu2^{WT}$ or myc-$\mu2^{S45A}$ were seeded on 10 cm diameter dish ($5x10^6$ cells/dish). After 24 h cells were washed 2 times with cold TBS-K buffer, harvested and lysed on ice for 15 min in lysis buffer (20 mM Tris pH 7.5, 150 mM NaCl, 0.5% CHAPS (3-((3-cholamidopropyl) dimethylammonio)-1-propanesulfonate) supplemented with protease and phosphatase inhibitors. The lysates were incubated with Pierce™ Anti-c-Myc Magnetic Beads (ThermoFisher Scientific, #88843) with rotation for 2 hours at room temperature. After this time beads were washed 4 times with washing buffer (20 mM Tris pH 7.5, 300 mM NaCl, 0.1% CHAPS), eluted in 2 times Laemmli sample buffer, and analyzed by Western blot.

Worm mobility and size

Approximately 10 young adult worms per replicate were placed onto NGM plates and were recorded for 2 min using the WormLab system (MBF Bioscience). The frame rate, exposure time, and gain were set to 7.5 frames per second, 0.0031 s, and 1, respectively. The track length and size of the individual worm were analyzed using the WormLab software (MBF Bioscience). The assay consisted of three independent biological replicates. 37-39 worms were recorded for one biological replicate.

Lifespan assay

Lifespan measurements were done from the young adult stage at 20°C on NGM plates containing 400 μM FUdR. During lifespan measurements, worms were scored daily for movement and pharyngeal pumping until death. Animals that crawled off the plate or exhibited baggy phenotype were censored from the experiment. The essay consisted of three independent biological replicates, with each replicate comprising 20 worms.

Egg-laying and hatching analysis

Age-synchronized hermaphrodites at the L4 developmental stage were picked for the experiment. Worms were cultured as single worms per 60 mm NGM plate, seeded with E. coli OP50. The assay consisted of three independent biological replicates, with each replicate comprising 10 worms. The experiment involved a 24-hour observation period during which we recorded the total egg production. Concurrently, we monitored the emergence of larvae to determine the success rate of hatching.

Statistical analysis

The exact number of repetitions of each experiment (N) and the number of cells (n) that were examined for the respective experiments are listed in the figure legends. The statistical analysis

was performed using GraphPad Prism 10 studio or Matlab. The exact statistical test that was used in the particular analysis is provided in the figure legend.

Acknowledgments

The authors thank all researchers listed in Materials and Methods for sharing reagents. We are also grateful to Prof. Juan Bonifacio for hosting AT in his lab and advising her on research directions, Volker Haucke, Martin Lehmann, Jan Brezovsky Marcel Mettlen, Zhiming Chen, and Carlos Eduardo Sequeiros Borja for helpful discussions. We also thank Agata Malinowska, Katarzyna Orzol and Roberto Pagano for help with experiments, and Alina Zielinska for technical assistance and support, Marcelina Firkowska, Marek Sarnacki and Angelika Jocek for laboratory management logistics.

This research was supported by Polish National Science Centre Preludium grant no. 2017/25/N/NZ3/01280 to AT. AT was partly financed by Polish National Science Centre Opus grants no. 2016/21/B/NZ3/03639 and 2017/27/B/NZ3/01358 to JJ. Work of AB was partly financed from Polish National Science Centre Opus grants no. 2016/21/B/NZ3/03639. JJ was partly financed by the TEAM grant from the Foundation for Polish Science (POIR.04.04.00-00-5CBE/17-00). The work of EL was financed from IIMCB statutory funds. The work of KM was partly financed from Polish National Science Centre Maestro grant 2020/38/A/NZ3/00447 to JJ. ARM was partly financed within the Parent-Bridge program of the Foundation for Polish Science, co-financed by the European Union under the European Regional Development Fund (POMOST/2013-7/10) and by I.3.4 Action of the Excellence Initiative - Research University Programme at the University of Warsaw. This research was also possible thanks to the IIMCB IN-MOL-CELL Infrastructure funded by the European Union – NextGenerationEU under National Recovery and Resilience Plan. IN-MOL-CELL Infrastructure was also funded by the European

Union under Horizon Europe (Project 101059801 - RACE) and by RACE-PRIME project carried out within the IRAP programme of the Foundation for Polish Science co-financed by the European Union under the European Funds for Smart Economy 2021-2027 (FENG)

Data availability

All data generated or analyzed during this study are included in this published article and its supplementary materials. Raw data from all quantitatively analyzed experiments are available from the corresponding authors upon reasonable request.

Author contributions

AT, AB, TW, WP, ARM and JJ designed the experiments. AT, AB, TW, KO, KJ, EL, KM1, MM1, ASz, ES, KM2, AG, and ARM performed the experiments. AGW performed in silico analysis. AT, AB, TW, KO, KJ, EL, MM1, ES, MM2, WP, ARM and JJ analyzed the data. AT, AB, AGW, WP, ARM and JJ wrote the manuscript. All authors read and approved the manuscript.

Declaration of interests

None of the authors have any financial or non-financial competing interests.

References

1. Collins BM, McCoy AJ, Kent HM, Evans PR, Owen DJ. Molecular architecture and functional model of the endocytic AP2 complex. Cell. 2002;109: 523–535.

2. Jackson LP, Kelly BT, McCoy AJ, Gaffry T, James LC, Collins BM, et al. A large-scale conformational change couples membrane recruitment to cargo binding in the AP2 clathrin adaptor complex. Cell. 2010;141: 1220–1229. doi:10.1016/j.cell.2010.05.006

3. Kadlecova Z, Spielman SJ, Loerke D, Mohanakrishnan A, Reed DK, Schmid SL. Regulation of clathrin-mediated endocytosis by hierarchical allosteric activation of AP2. J Cell Biol. 2017;216: 167–179. doi:10.1083/jcb.201608071

4. Beacham GM, Partlow EA, Lange JJ, Hollopeter G. NECAPs are negative regulators of the AP2 clathrin adaptor complex. Elife. 2018;7: e32242. doi:10.7554/eLife.32242

5. Kelly BT, McCoy AJ, Späte K, Miller SE, Evans PR, Höning S, et al. A structural explanation for the binding of endocytic dileucine motifs by the AP2 complex. Nature. 2008;456: 976–979. doi:10.1038/nature07422

6. Kovtun O, Dickson VK, Kelly BT, Owen DJ, Briggs JAG. Architecture of the AP2/clathrin coat on the membranes of clathrin-coated vesicles. Sci Adv. 2020;6: eaba8381. doi:10.1126/sciadv.aba8381

7. Wrobel AG, Kadlecova Z, Kamenicky J, Yang J-C, Herrmann T, Kelly BT, et al. Temporal Ordering in Endocytic Clathrin-Coated Vesicle Formation via AP2 Phosphorylation. Dev Cell. 2019;50: 494-508.e11. doi:10.1016/j.devcel.2019.07.017

8. Korolchuk V, Banting G. Kinases in clathrin-mediated endocytosis. Biochem Soc Trans. 2003;31: 857–860. doi:10.1042/bst0310857

9. Liberali P, Rämö P, Pelkmans L. Protein kinases: starting a molecular systems view of endocytosis. Annu Rev Cell Dev Biol. 2008;24: 501–523. doi:10.1146/annurev.cellbio.041008.145637

10. Partlow EA, Baker RW, Beacham GM, Chappie JS, Leschziner AE, Hollopeter G. A structural mechanism for phosphorylation-dependent inactivation of the AP2 complex. Elife. 2019;8: e50003. doi:10.7554/eLife.50003

11. Fingerhut A, von Figura K, Honing S. Binding of AP2 to sorting signals is modulated by AP2 phosphorylation. J Biol Chem. 2001;276: 5476–5482. doi:10.1074/jbc.M009516200

12. Ricotta D, Conner SD, Schmid SL, von Figura K, Honing S. Phosphorylation of the AP2 mu subunit by AAK1 mediates high affinity binding to membrane protein sorting signals. J Cell Biol. 2002;156: 791–795. doi:10.1083/jcb.200111068

13. Liu J, Du J, Wang Y. CDK5 inhibits the clathrin-dependent internalization of TRPV1 by phosphorylating the clathrin adaptor protein AP2µ2. Sci Signal. 2019;12: eaaw2040. doi:10.1126/scisignal.aaw2040

14. Karalis V, Bateup HS. Current Approaches and Future Directions for the Treatment of mTORopathies. Dev Neurosci. 2021;43: 143–158. doi:10.1159/000515672

15. Switon K, Kotulska K, Janusz-Kaminska A, Zmorzynska J, Jaworski J. Molecular neurobiology of mTOR. Neuroscience. 2017;341: 112–153. doi:10.1016/j.neuroscience.2016.11.017

16. Bonucci M, Kuperwasser N, Barbe S, Koka V, De Villeneuve D, Zhang C, et al. mTOR and S6K1 drive polycystic kidney by the control of Afadin-dependent oriented cell division. Nat Commun. 2020;11: 3200. doi:10.1038/s41467-020-16978-z

17. Fricke AL, Mühlhäuser WWD, Reimann L, Zimmermann JP, Reichenbach C, Knapp B, et al. Phosphoproteomics Profiling Defines a Target Landscape of the Basophilic Protein Kinases AKT, S6K, and RSK in Skeletal Myotubes. J Proteome Res. 2023;22: 768–789. doi:10.1021/acs.jproteome.2c00505

18. Fumagalli S, Pende M. S6 kinase 1 at the central node of cell size and ageing. Front Cell Dev Biol. 2022;10: 949196. doi:10.3389/fcell.2022.949196

19. Grahammer F, Ramakrishnan SK, Rinschen MM, Larionov AA, Syed M, Khatib H, et al. mTOR Regulates Endocytosis and Nutrient Transport in Proximal Tubular Cells. JASN. 2017;28: 230–241. doi:10.1681/ASN.2015111224

20. Malik AR, Urbanska M, Macias M, Skalecka A, Jaworski J. Beyond control of protein translation: what we have learned about the non-canonical regulation and function of mammalian target of rapamycin (mTOR). Biochim Biophys Acta. 2013;1834: 1434–48. doi:10.1016/j.bbapap.2012.12.010

21. Switon K, Kotulska K, Janusz-Kaminska A, Zmorzynska J, Jaworski J. Tuberous sclerosis complex: From molecular biology to novel therapeutic approaches. IUBMB Life. 2016;68: 955–962. doi:10.1002/iub.1579

22. Loerke D, Mettlen M, Yarar D, Jaqaman K, Jaqaman H, Danuser G, et al. Cargo and Dynamin Regulate Clathrin-Coated Pit Maturation. Hughson F, editor. PLoS Biol. 2009;7: e1000057. doi:10.1371/journal.pbio.1000057

23. Merrifield CJ, Feldman ME, Wan L, Almers W. Imaging actin and dynamin recruitment during invagination of single clathrin-coated pits. Nat Cell Biol. 2002;4: 691–698. doi:10.1038/ncb837

24. Mettlen M, Danuser G. Imaging and Modeling the Dynamics of Clathrin-Mediated Endocytosis. Cold Spring Harbor Perspectives in Biology. 2014;6: a017038–a017038. doi:10.1101/cshperspect.a017038

25. Aguet F, Antonescu CN, Mettlen M, Schmid SL, Danuser G. Advances in Analysis of Low Signal-to-Noise Images Link Dynamin and AP2 to the Functions of an Endocytic Checkpoint. Developmental Cell. 2013;26: 279–291. doi:10.1016/j.devcel.2013.06.019

26. Loerke D, Mettlen M, Schmid SL, Danuser G. Measuring the Hierarchy of Molecular Events During Clathrin-Mediated Endocytosis. Traffic. 2011;12: 815–825. doi:10.1111/j.1600-0854.2011.01197.x

27. Mettlen M, Chen P-H, Srinivasan S, Danuser G, Schmid SL. Regulation of Clathrin-Mediated Endocytosis. Annu Rev Biochem. 2018;87: 871–896. doi:10.1146/annurev-biochem-062917-012644

28. Jastrzębski K, Zdżalik-Bielecka D, Mamińska A, Kalaidzidis Y, Hellberg C, Miaczynska M. Multiple routes of endocytic internalization of PDGFRβ contribute to PDGF-induced STAT3 signaling. Journal of Cell Science. 2017;130: 577–589. doi:10.1242/jcs.191213

29. Chen Y, Gershlick DC, Park SY, Bonifacino JS. Segregation in the Golgi complex precedes export of endolysosomal proteins in distinct transport carriers. J Cell Biol. 2017;216: 4141–4151. doi:10.1083/jcb.201707172

30. Motley AM, Berg N, Taylor MJ, Sahlender DA, Hirst J, Owen DJ, et al. Functional Analysis of AP-2 α and μ2 Subunits. Mol Biol Cell. 2006;17: 5298–5308. doi:10.1091/mbc.E06-05-0452

31. Gu M, Schuske K, Watanabe S, Liu Q, Baum P, Garriga G, et al. Mu2 adaptin facilitates but is not essential for synaptic vesicle recycling in Caenorhabditis elegans. J Cell Biol. 2008;183: 881–892. doi:10.1083/jcb.200806088

32. Gu M, Liu Q, Watanabe S, Sun L, Hollopeter G, Grant BD, et al. AP2 hemicomplexes contribute independently to synaptic vesicle endocytosis. Elife. 2013;2: e00190. doi:10.7554/eLife.00190

33. Skop AR, Liu H, Yates J, Meyer BJ, Heald R. Dissection of the Mammalian Midbody Proteome Reveals Conserved Cytokinesis Mechanisms. Science. 2004;305: 61–66. doi:10.1126/science.1097931

34. Page AP, Johnstone IL. The cuticle. WormBook. 2007; 1–15. doi:10.1895/wormbook.1.138.1

35. Cho JY, Choi T-W, Kim SH, Ahnn J, Lee S-K. Morphological Characterization of small, dumpy, and long Phenotypes in Caenorhabditis elegans. Molecules and Cells. 2021;44: 160–167. doi:10.14348/molcells.2021.2236

36. Beacham GM, Partlow EA, Hollopeter G. Conformational regulation of AP1 and AP2 clathrin adaptor complexes. Traffic. 2019;20: 741–751. doi:10.1111/tra.12677

37. Weinberg J, Drubin DG. Clathrin-mediated endocytosis in budding yeast. Trends Cell Biol. 2012;22: 1–13. doi:10.1016/j.tcb.2011.09.001

38. Kaksonen M, Roux A. Mechanisms of clathrin-mediated endocytosis. Nat Rev Mol Cell Biol. 2018;19: 313–326. doi:10.1038/nrm.2017.132

39. Arif A, Jia J, Willard B, Li X, Fox PL. Multisite Phosphorylation of S6K1 Directs a Kinase Phospho-code that Determines Substrate Selection. Molecular Cell. 2019;73: 446-457.e6. doi:10.1016/j.molcel.2018.11.017

40. Lai K-O, Liang Z, Fei E, Huang H, Ip NY. Cyclin-dependent Kinase 5 (Cdk5)-dependent Phosphorylation of p70 Ribosomal S6 Kinase 1 (S6K) Is Required for Dendritic Spine Morphogenesis. J Biol Chem. 2015;290: 14637–14646. doi:10.1074/jbc.M114.627117

41. Deguil J, Peraultpochat M, Chavant F, Lafaychebassier C, Fauconneau B, Pain S. Activation of the protein p7OS6K via ERK phosphorylation by cholinergic muscarinic receptors stimulation in human neuroblastoma cells and in mice brain. Toxicology Letters. 2008;182: 91–96. doi:10.1016/j.toxlet.2008.08.012

42. Guégan J-P, Ezan F, Gailhouste L, Langouët S, Baffet G. MEK1/2 Overactivation Can Promote Growth Arrest by Mediating ERK1/2-Dependent Phosphorylation of p70S6K: p70S6K AND MAPK-INDUCED GROWTH ARREST. J Cell Physiol. 2014;229: 903–915. doi:10.1002/jcp.24521

43. Heberle AM, Razquin Navas P, Langelaar-Makkinje M, Kasack K, Sadik A, Faessler E, et al. The PI3K and MAPK/p38 pathways control stress granule assembly in a hierarchical manner. Life Sci Alliance. 2019;2: e201800257. doi:10.26508/lsa.201800257

44. Iijima Y, Laser M, Shiraishi H, Willey CD, Sundaravadivel B, Xu L, et al. c-Raf/MEK/ERK Pathway Controls Protein Kinase C-mediated p70S6K Activation in Adult Cardiac Muscle Cells. Journal of Biological Chemistry. 2002;277: 23065–23075. doi:10.1074/jbc.M200328200

45. Wu X, Xie W, Xie W, Wei W, Guo J. Beyond controlling cell size: functional analyses of S6K in tumorigenesis. Cell Death Dis. 2022;13: 1–19. doi:10.1038/s41419-022-05081-4

46. Chen M, Wan L, Zhang J, Zhang J, Mendez L, Clohessy JG, et al. Deregulated PP1α phosphatase activity towards MAPK activation is antagonized by a tumor suppressive failsafe mechanism. Nat Commun. 2018;9: 159. doi:10.1038/s41467-017-02272-y

47. Haucke V. Phosphoinositide regulation of clathrin-mediated endocytosis. Biochem Soc Trans. 2005;33: 1285–1289. doi:10.1042/BST0331285

48. Rebholz H, Panasyuk G, Fenton T, Nemazanyy I, Valovka T, Flajolet M, et al. Receptor association and tyrosine phosphorylation of S6 kinases. The FEBS Journal. 2006;273: 2023–2036. doi:10.1111/j.1742-4658.2006.05219.x

49. Rahmani S, Defferrari MS, Wakarchuk WW, Antonescu CN. Energetic adaptations: Metabolic control of endocytic membrane traffic. Traffic. 2019;20: 912–931. doi:10.1111/tra.12705

50. Antonescu CN, McGraw TE, Klip A. Reciprocal Regulation of Endocytosis and Metabolism. Cold Spring Harb Perspect Biol. 2014;6: a016964. doi:10.1101/cshperspect.a016964

51. Zou Z, Tao T, Li H, Zhu X. mTOR signaling pathway and mTOR inhibitors in cancer: progress and challenges. Cell & Bioscience. 2020;10: 31. doi:10.1186/s13578-020-00396-1

52. Sorkin A, von Zastrow M. Endocytosis and signalling: intertwining molecular networks. Nat Rev Mol Cell Biol. 2009;10: 609–622. doi:10.1038/nrm2748

53. Hupalowska A, Miaczynska M. The new faces of endocytosis in signaling. Traffic. 2012;13: 9–18. doi:10.1111/j.1600-0854.2011.01249.x

54. Miaczynska M, Pelkmans L, Zerial M. Not just a sink: endosomes in control of signal transduction. Curr Opin Cell Biol. 2004;16: 400–406. doi:10.1016/j.ceb.2004.06.005

55. Banushi B, Joseph SR, Lum B, Lee JJ, Simpson F. Endocytosis in cancer and cancer therapy. Nat Rev Cancer. 2023;23: 450–473. doi:10.1038/s41568-023-00574-6

56. Mellman I, Yarden Y. Endocytosis and Cancer. Cold Spring Harb Perspect Biol. 2013;5: a016949. doi:10.1101/cshperspect.a016949

57. Guo H, Zhou C, Zheng M, Zhang J, Wu H, He Q, et al. Insights into the role of derailed endocytic trafficking pathway in cancer: From the perspective of cancer hallmarks. Pharmacological Research. 2024;201: 107084. doi:10.1016/j.phrs.2024.107084

58. Chan ET, Kural C. Targeting endocytosis to sensitize cancer cells to programmed cell death. Biochemical Society Transactions. 2024;52: 1703–1713. doi:10.1042/BST20231332

59. de Boer E, Rodriguez P, Bonte E, Krijgsveld J, Katsantoni E, Heck A, et al. Efficient biotinylation and single-step purification of tagged transcription factors in mammalian cells and transgenic mice. Proc Natl Acad Sci U S A. 2003;100: 7480–5. doi:10.1073/pnas.1332608100

60. Swiech L, Blazejczyk M, Urbanska M, Pietruszka P, Dortland BR, Malik AR, et al. CLIP-170 and IQGAP1 Cooperatively Regulate Dendrite Morphology. J Neurosci. 2011;31: 4555–4568. doi:10.1523/JNEUROSCI.6582-10.2011

61. Pawlik B, Grabia S, Smyczyńska U, Fendler W, Dróżdż I, Liszewska E, et al. MicroRNA Expression Profile in TSC Cell Lines and the Impact of mTOR Inhibitor. IJMS. 2022;23: 14493. doi:10.3390/ijms232214493

62. Li MZ, Elledge SJ. Harnessing homologous recombination in vitro to generate recombinant DNA via SLIC. Nature methods. 2007;4: 251–6. doi:10.1038/nmeth1010

63. Brenner S. THE GENETICS OF *CAENORHABDITIS ELEGANS*. Genetics. 1974;77: 71–94. doi:10.1093/genetics/77.1.71

64. Dokshin GA, Ghanta KS, Piscopo KM, Mello CC. Robust Genome Editing with Short Single-Stranded and Long, Partially Single-Stranded DNA Donors in *Caenorhabditis elegans*. Genetics. 2018;210: 781–787. doi:10.1534/genetics.118.301532

65. Wróbel M, Cendrowski J, Szymańska E, Grębowicz-Maciukiewicz M, Budick-Harmelin N, Macias M, et al. ESCRT-I fuels lysosomal degradation to restrict TFEB/TFE3 signaling via the Rag-mTORC1 pathway. Life Sci Alliance. 2022;5: e202101239. doi:10.26508/lsa.202101239

66. Gozdz A, Nikolaienko O, Urbanska M, Cymerman IA, Sitkiewicz E, Blazejczyk M, et al. GSK3α and GSK3β Phosphorylate Arc and Regulate its Degradation. Front Mol Neurosci. 2017;10: 192. doi:10.3389/fnmol.2017.00192

67. Madeira F, Pearce M, Tivey ARN, Basutkar P, Lee J, Edbali O, et al. Search and sequence analysis tools services from EMBL-EBI in 2022. Nucleic Acids Research. 2022;50: W276–W279. doi:10.1093/nar/gkac240

68. Waterhouse AM, Procter JB, Martin DMA, Clamp M, Barton GJ. Jalview Version 2—a multiple sequence alignment editor and analysis workbench. Bioinformatics. 2009;25: 1189–1191. doi:10.1093/bioinformatics/btp033

Figures and Figure Legends

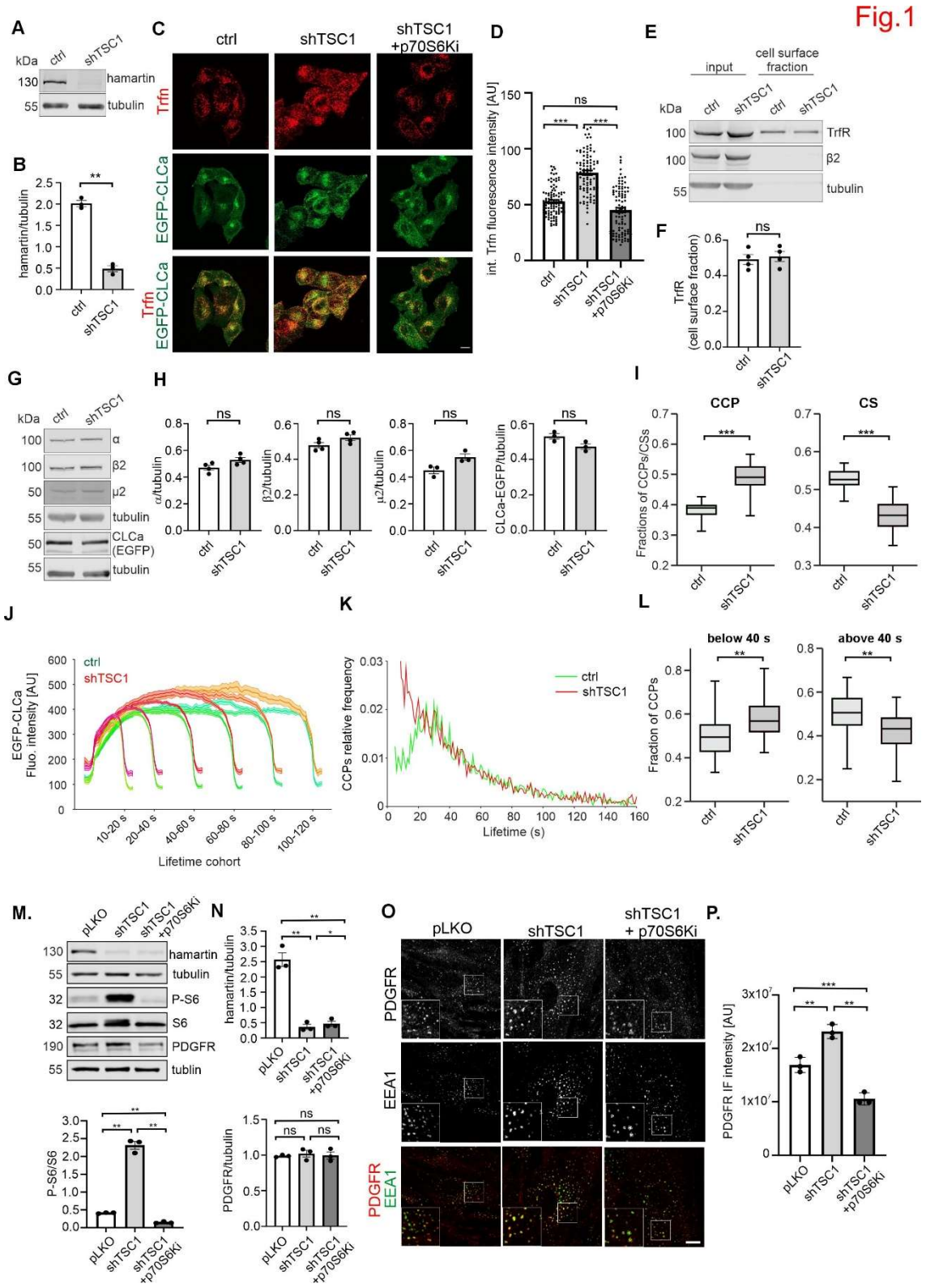

Figure 1. Cargo internalization via CME is upregulated in cells with overactive p70S6K.

A. Western blot showing levels of endogenous hamartin in HeLa cells stably expressing EGFP-CLCa only (ctrl) or with TSC1 shRNA (shTSC1). **B.** Quantitative analysis of hamartin levels. N = 3 independent experiments. $^{**}p < 0.01$ (paired t-test; t = 10.81, df = 2). **C.** Representative confocal images of cells after 5-minute uptake of Alexa Fluor 647-labeled transferrin (Trfn, red). HeLa cells stably expressing EGFP-CLCa only (ctrl) or together with TSC1 shRNA (shTSC1) were serum-starved and treated with 0.1% DMSO or 10 µM p70S6K inhibitor for 2 h before transferrin uptake. EGFP-CLCa is shown in green. Scale bar = 10 µm. **D.** Analysis of immunofluorescence signal of internalized Alexa Fluor 647-conjugated transferrin normalized to cell area in cells treated as in *C*. The data are shown as the mean value ± SEM. N = 2 independent experiments. Number of cells (n) = 101 (ctrl), 93 (shTSC1), 96 (shTSC1 +p70S6Ki). $^{***}p < 0.001$, *ns* – non-significant (Kruskal Wallis test [H = 107.3] with Dunn's multiple comparisons test). **E.** Western blot showing cell membrane levels of TrfR in HeLa cells as in *A*, analyzed by pull-down of biotinylated cell surface proteins. **F.** Quantitative analysis of TrfR surface expression. N = 4 independent experiments. *ns* – non-significant (paired t-test; [t = 0.2918, df = 3]). **G.** Western blot showing expression level of AP2 subunits and clathrin light chain fused with EGFP (EGFP-CLCa) in cell lines as in *A*. **H.** Quantitative analysis of AP2 α, β2, µ2 subunits, and CLCa-EGFP levels. N = 4 independent experiments for α, β2. N = 3 independent experiments for µ2 and CLCa-EGFP. *ns* – non-significant (paired t-test; α [t = 1.587, df = 3], β2 [t = 1.376, df = 3], µ2 [t = 1.994, df = 2], CLCa-EGFP [t = 1.848, df = 2]). **I.** Fractions of all detected CCPs and CSs found among all valid tracks (ctrl: number of analyzed movies (n) = 26, number of total valid tracks = 27800; shTSC1: number of analyzed movies (n) = 30, number of total valid tracks = 25875). Box plots show medians, 25th and 75th percentiles, and outermost data points. $^{***}p < 0.001$ Matlab ranksum (p value 1.92e-09 for CCPs and 5.58e-10 for CSs). **J.** Clathrin fluorescence intensity in CCPs lifetime cohorts of control cells (green) and cells with *TSC1* knockdown (red). Intensities are shown as mean ± SE. **K.** Lifetime distributions of all CCPs found in HeLa control cells (green) and with *TSC1* knockdown (red). **L.** Fractions of CCPs with time of living below and above 40 s for control and shTSC1-expressing HeLa cells. Box plots show medians, 25th and 75th percentiles, and outermost data points. $^{**}p < 0.01$ Matlab ranksum (p value 0.0039 for "below 40 s" and 0.0039 for "above 40 s"). **M.** Western blot showing levels of endogenous hamartin, P-S6 (235/236), S6, PDGFR and tubulin in CCD-1070Sk cells transduced with control (pLKO) or shTSC1-encoding lentiviral vector, serum-starved and treated with 0.1% DMSO or 10 µM p70S6K inhibitor for 2 h. **N.** Quantitative analysis of hamartin, P-S6 (S235/236) and PDGFR levels. N = 3 independent experiments. $^{**}p < 0.01$, $^{*}p < 0.05$, *ns* – non-significant (RM one way ANOVA followed by Tukey's multiple comparisons test). **O.** Representative confocal images of CCD-1070Sk treated as in *M*, stimulated with PDGF for 15 minutes and immunofluorescently stained for PDGFR (red) and EEA1 (green). Scale bar = 10 µm. **P.** Analysis of PDGFR endocytic immunofluorescence signal intensity in cells treated as in *O*. The data are shown as the mean value ± SEM. N = 3 independent experiments. $^{***}p < 0.001$, $^{**}p < 0.01$ (One-way ANOVA followed by Tukey's multiple comparisons test, pLKO vs. shTSC1: q = 8.367, df = 6; pLKO vs. shTSC1+p70S6Ki: q= 8.451, df = 6; shTSC1 vs. shTSC1+p70S6Ki: q = 16.82, df = 6).

Fig.2

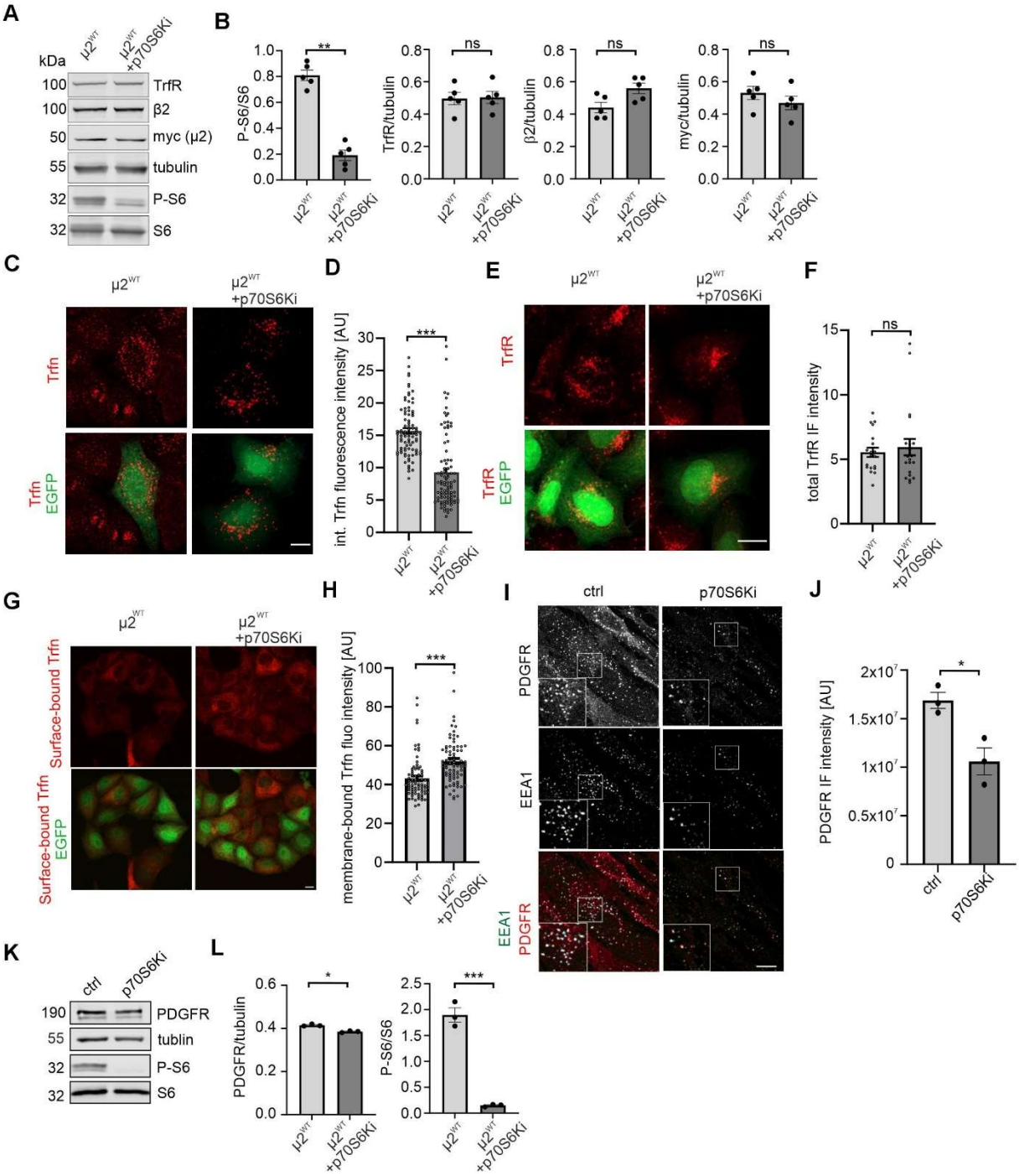

Figure 2. Efficient CME requires p70S6K activity in cells with basal mTOR activity.

A. Western blot showing levels of endogenous TrfR, β2, S6, P-S6, and tubulin in HeLa cells transfected with plasmids encoding myc-μ2^{WT} and EGFP, and treated with 0.1% DMSO or p70S6K inhibitor (p70S6Ki, 10 μM, 2 h) after overnight starvation in FBS-free medium. **B.** Quantitative analysis of TrfR, β2, myc-μ2, and P-S6 (S235/236) levels. N = 5 independent

experiments. $**p < 0.01$, *ns* – non-significant (paired t-test; TrfR [t = 0.08916, df = 4], β2 [t = 1.842, df = 4], myc-μ2 [t = 0.7428, df = 4], P-S6 [t = 7.540, df = 4]). **C.** Representative confocal images of cells after transferrin uptake. HeLa KO μ2 transfected with plasmids encoding myc-$\mu2^{WT}$ and EGFP were treated for 2 h with 0.1% DMSO or 10 μM p70S6Ki before 5-minute incubation with Alexa Fluor 647-labeled transferrin. Transferrin is seen in red and EGFP in green. Scale bar = 10 μm. **D.** Quantification of the fluorescence signal intensity of transferrin internalized by cells treated as in *C*. Data are presented as mean ± SEM. $N = 3$ independent experiments. Number of analyzed cells (n) = 80 ($\mu2^{WT}$), 87 ($\mu2^{WT}$ + p70S6Ki), $***p < 0.001$ (Student's t test for independent samples; t = 8.728, df = 174). **E.** Representative confocal images of HeLa KO μ2 cells transfected with plasmids encoding myc-$\mu2^{WT}$ and EGFP, serum-starved and treated for 2 h with 0.1% DMSO, or 10 μM p70S6Ki. Cells were immunofluorescently stained for transferrin receptor (TrfR, red) and EGFP (green). Scale bar = 10 μm. **F.** Quantification of the TrfR fluorescence signal intensity level in cells treated as in *E*. Data are presented as mean ± SEM. $N = 2$ independent experiments. Number of analyzed cells (n) = 19 (DMSO), 21 (p70S6Ki). *ns* – non-significant (Mann-Whitney test, U = 195). **G.** Representative confocal images of Alexa Fluor 647-conjugated transferrin (red) bound to cell surface of HeLa KO μ2 cells transfected with plasmids encoding myc-$\mu2^{WT}$ and EGFP (green), serum starved and treated with 0.1% DMSO or p70S6Ki (10 μM, 2 h). Scale bar = 10 μm. **H.** Quantification of the mean immunofluorescence intensity of transferrin conjugated with Alexa Fluor 647 bound to cell surface. Cells were treated as in *G*. The data are expressed as mean ± SEM. $N = 4$ independent experiments. Number of analyzed cells (n) = 78 ($\mu2^{WT}$), 81 ($\mu2^{WT}$ + p70S6Ki). $***p < 0.001$ (Mann-Whitney test, U = 1487). **I.** Representative confocal images of CCD-1070Sk cells that were serum-starved, treated with 0.1% DMSO (ctrl) or 10 μM p70S6Ki for 2 h and stimulated with PDGF for 15 minutes. Cells were immunofluorescently stained for PDGFR (red) and EEA1 (green). Scale bar = 10 μm. **J.** Analysis of endocytic PDGFR immunofluorescence signal intensity in cells treated as in *I*. The data are shown as the mean value ± SEM. $N = 3$ independent experiments. $*p < 0.05$ (unpaired t-test for, t = 3,894, df = 4). **K.** Western blot showing levels of P-S6 (235/236), S6, PDGFR, and tubulin in CCD-1070Sk cells that were serum-starved and treated with 0.1% DMSO (ctrl) or 10 μM p70S6Ki for 2 h. **L.** Quantitative analysis of PDGFR and P-S6 (S235/236) levels in cells treated as in *K*. $N = 3$ independent experiments. $*p < 0.05$,$***p < 0.001$ (paired t-test, PDGFR [t = 5.779, df = 2], P-S6 [t = 11.65, df = 2]).

Fig.3

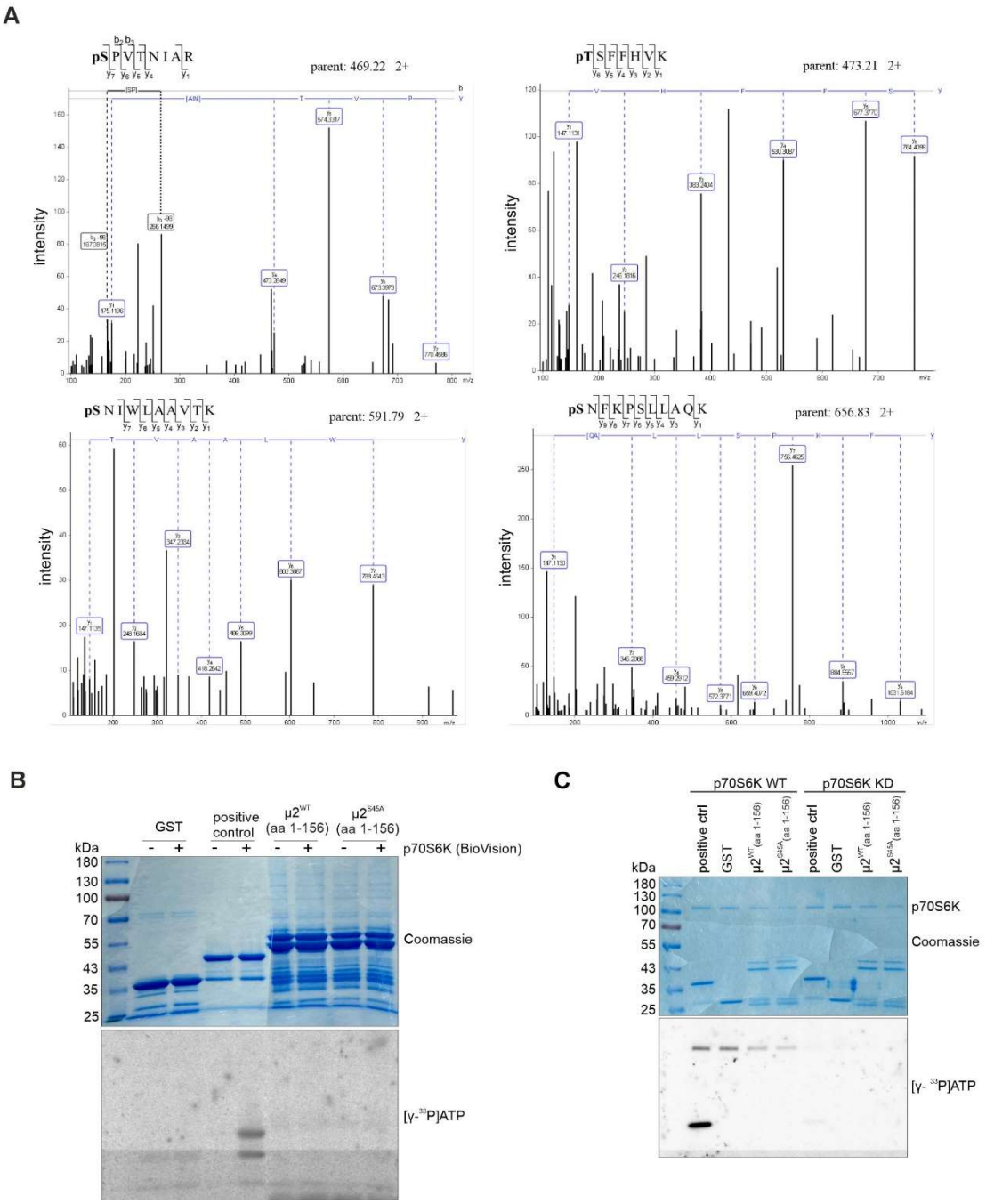

Figure 3. p70S6K indirectly regulates μ2 phosphorylation.

A. Novel p70S6K-dependent phosphorylation sites are present in μ2 protein. Representative fragmentation of peptides that encompass the phosphorylated serine 45 (S45), threonine 53 (T53), serine 61 (S61), and serine 309 (S309) residues. The μ2 protein was purified from HEK293T cells expressing GFP-Avi-tag-μ2 and BirA, serum-starved, and treated for 2 h with DMSO (0.1%) or p70S6Ki (10 μM). **B.** Results of kinase assay using active p70S6K (Biovision, 7725) and fragments (aa 1-156) of recombinant $\mu2^{WT}$ or $\mu2^{S45A}$, His-tagged C-terminal fragment of RPS6

(positive control) or GST (negative control) as substrates. The upper panel shows Coomassie R-250 staining of SDS-PAGE gels with the analyzed proteins. The lower panel shows the radioactive signal level of [γ-33P] ATP incorporated into the analyzed proteins. A representative example from $N = 3$ independent experiments is shown. **C.** Results of kinase assay using wild type (WT) or kinase-dead (KD) p70S6K and fragments (aa 1-156) of recombinant $\mu2^{WT}$ or $\mu2^{S45A}$, His-tagged C-terminal fragment of RPS6 (positive control) or GST (negative control) as substrates. p70S6K (WT or KD) was pulled down from HEK293T cells co-transfected with plasmids carrying p70S6KBioGFP WT or p70S6KBioGFP KD together with a plasmid carrying BirA. The upper panel shows Coomassie R-250 staining of SDS-PAGE gels with the analyzed proteins. The lower panel shows the radioactive signal level of [γ-33P] ATP incorporated into the analyzed proteins. A representative example from $N = 5$ independent experiments is shown.

Fig.4

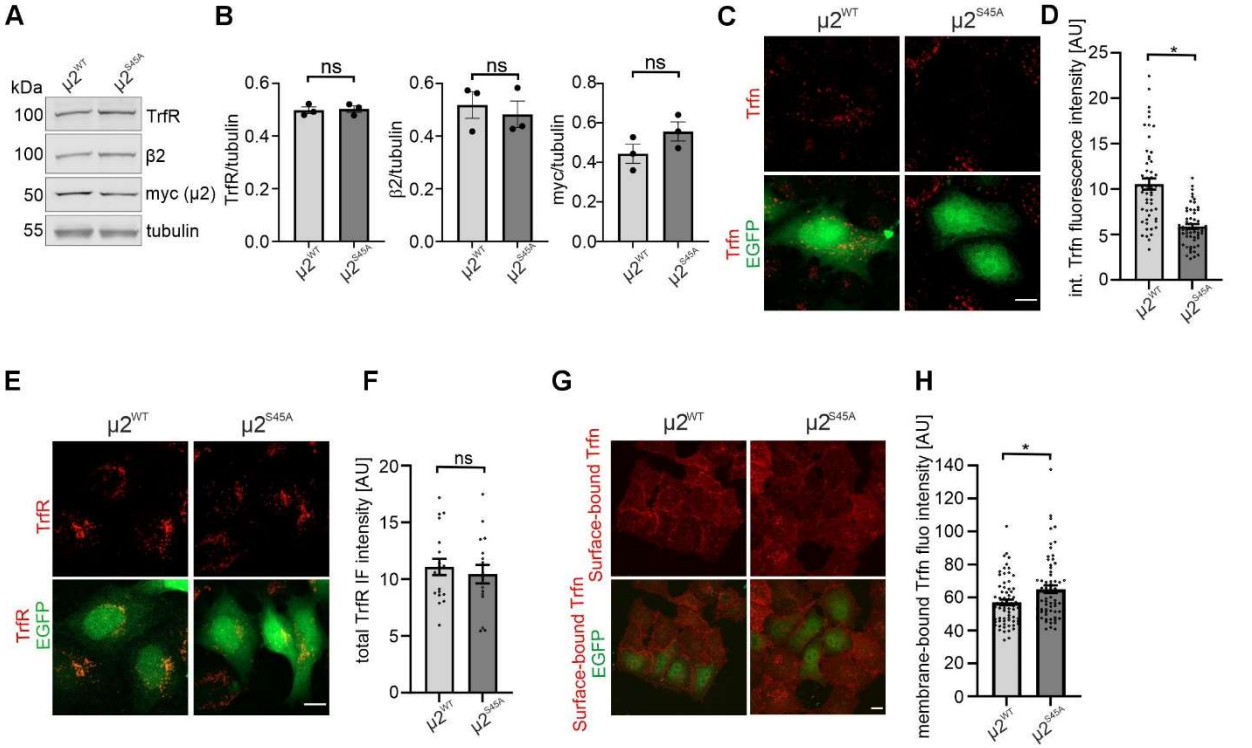

Figure 4. Lack of S45 phosphorylation of μ2 mimics the effects of p70S6K inhibition on transferrin internalization.

A. Western blot analysis of TrfR, β2, myc-μ2 and tubulin in protein lysates obtained from HeLa KO μ2 transfected with a plasmid encoding myc-$\mu2^{WT}$ or myc-$\mu2^{S45A}$. **B.** Quantitative analysis of TrfR, β2, and myc-μ2 levels. $N = 3$ independent experiments. ns – non-significant (paired t-test; TrfR [$t = 0.1878$, $df = 2$], β2 [$t = 0.3531$, $df = 2$], myc-μ2 [$t = 1.167$, $df = 2$]). **C.** Representative images of HeLa KO μ2 transfected with plasmids encoding myc-$\mu2^{WT}$ or myc-$\mu2^{S45A}$ together with EGFP, after 5-minute uptake of Alexa Fluor 647-labeled transferrin (red). EGFP is shown in green. Scale bar = 10 μm. **D.** Quantification of the mean fluorescence signal intensity of internalized

Alexa Fluor 647-conjugated transferrin in cells treated as in *C*. Data are presented as mean ± SEM. $N = 3$ independent experiments. Number of analyzed cells (n) =54 cells ($\mu2^{WT}$), 58 cells ($\mu2^{S45A}$), ***$p < 0.001$ (Mann-Whitney test, U=509). **E.** Representative confocal images of HeLa KO μ2 transfected with plasmids encoding myc-$\mu2^{WT}$ or myc-$\mu2^{S45A}$ together with EGFP, immunofluorescently stained for TrfR (red). Scale bar = 10 μm. **F.** Quantification of TrfR fluorescence signal intensity level in cells treated as in *E*. Mean ± SEM is shown. $N = 2$ independent experiments. Number of analyzed cells (n) = 19 ($\mu2^{WT}$), 17 ($\mu2^{S45A}$). *ns* -non-significant, (Student's t-test, t = 0.5813, df = 34). **G.** Representative confocal images of cell surface-bound transferrin conjugated with Alexa Fluor 647 (red) in HeLa KO μ2 cells transfected with plasmids encoding myc-$\mu2^{WT}$ or myc-$\mu2^{S45A}$ and EGFP (green). Scale bar = 10 μm. **H.** Quantification of the mean fluorescence intensity of transferrin conjugated with Alexa Fluor 647 bound to cell surface in cells treated as in *G*. Mean ± SEM is shown. $N = 4$ independent experiments. Number of analyzed cells (n) = 68 ($\mu2^{WT}$), 67 ($\mu2^{S45A}$). *$p < 0.05$ (Mann-Whitney test, U = 1729).

Fig.5

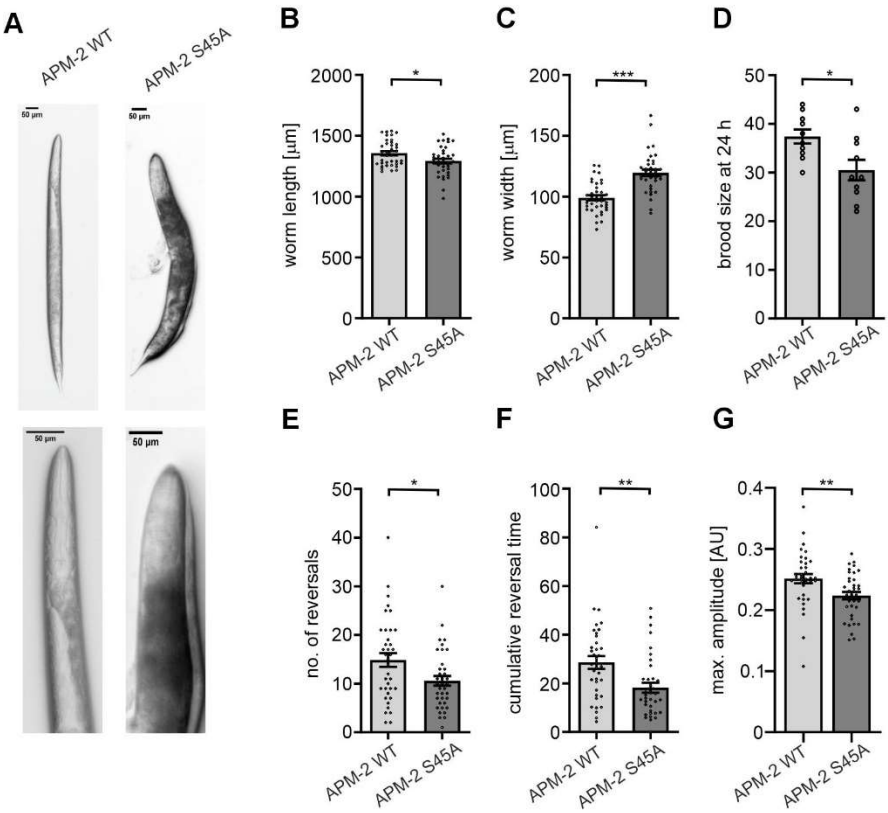

Figure 5. Substitution of serine 45 to alanine leads to apm-2 loss-of-function-like phenotypes in *C. elegans*.

A. Representative images of young adult *C. elegans* heads: wild type (N2) and APM-2S45A mutant. Scale bar = 50 μm. **B** and **C.** Comparison of the length and width between control (WT –

wild type, N2) and APM-2S45A animals. *$p < 0.05$ (Mann–Whitney test, U = 492), ***$p < 0.001$ (unpaired t-test, t = 6.026, df = 72). **D.** The number of eggs laid by wild-type (N2) and APM-2S45A worms after a 24-hour egg-laying period. *$p < 0.05$ (unpaired t-test, t = 2.697, df = 18). **E-G.** Number of reversals, cumulative reversal time and max. amplitude of the sinusoidal movement of wild-type (N2) and APM-2S45A worms measured by the WormLab system (MBF Bioscience). *$p < 0.05$, **$p < 0.01$ (Mann–Whitney test, [E] U = 485, [F] U = 402.5, [G] U = 399).

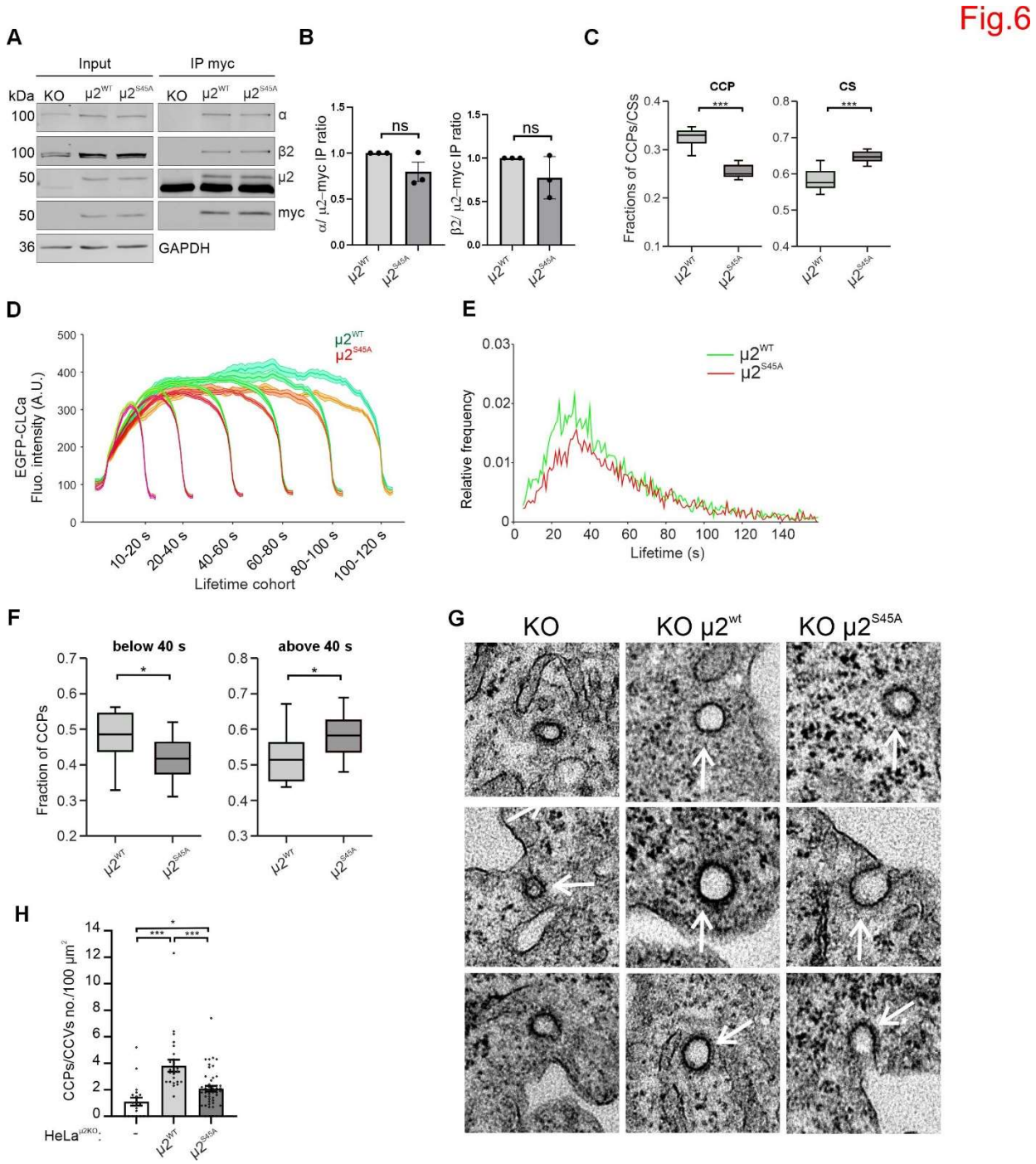

Figure 6. Phosphorylation of S45 of μ2 is needed for the effective formation of clathrin-coated pits.

A. Western blot showing co-immunoprecipitation of myc-μ2 with other AP2 subunits: α and β2 from HeLa KO μ2 cells stably expressing EGFP-CLCa and myc-μ2^{WT} or myc- μ2^{S45A}. Input, 10% of lysate used for immunoprecipitation. Shown is a representative example of *N= 3* independent experiments. **B.** Quantitative analysis of immunoprecipitated AP2 α and β2 subunits. *N* = 3

independent experiments. *ns* – non-significant (one sample t test; α [t=1,940, df=2], β2 [t=1,602, df=2]). **C.** Fractions of all detected subthreshold CCPs and CSs for cells expressing myc-$\mu2^{WT}$ or myc-$\mu2^{S45A}$ ($\mu2^{WT}$: number of analyzed movies = 12, number of total valid tracks = 28541, $\mu2^{S45A}$: number of analyzed movies = 12, number of total valid tracks = 26194). Box plots show medians, 25th and 75th percentiles, and outermost data points. ***$p < 0.001$ Matlab ranksum (p value 3.66e-05 for CCPs and 9.73e-05 for CSs). **D.** Clathrin fluorescence intensity in CCPs lifetime cohorts of cells expressing myc-$\mu2^{WT}$ (green) or myc-$\mu2^{S45A}$ (red). Intensities are shown as mean ± SE. **E.** Lifetime distributions of all CCPs found in cells expressing myc-$\mu2^{WT}$ (green) or myc-$\mu2^{S45A}$ (red). **F.** Fractions of CCPs with time of living below and above 40 s in cells expressing myc-$\mu2^{WT}$ or myc-$\mu2^{S45A}$. Box plots show medians, 25th and 75th percentiles, and outermost data points. *$p < 0.05$ Matlab ranksum, (p value 0.035 for "below 40 s" and 0.035 for "above 40 s"). **G.** Electron microscopy images of CCPs in HeLa KO, HeLa KO μ2 myc-$\mu2^{WT}$ or HeLa KO μ2 myc-$\mu2^{S45A}$. CCPs and CCVs are pointed with arrows. **H.** Quantification of CCPs/CCVs number from electron microscopy images. Error bars represent ± SEM, n =20 cells (KO), 25 cells (KO $\mu2^{WT}$), 45 cells (KO $\mu2^{S45A}$). ***$p < 0.001$; *$p < 0.05$ (Kruskal Wallis test [H=28.68] followed by multiple comparisons Dunn's test).

Fig.7

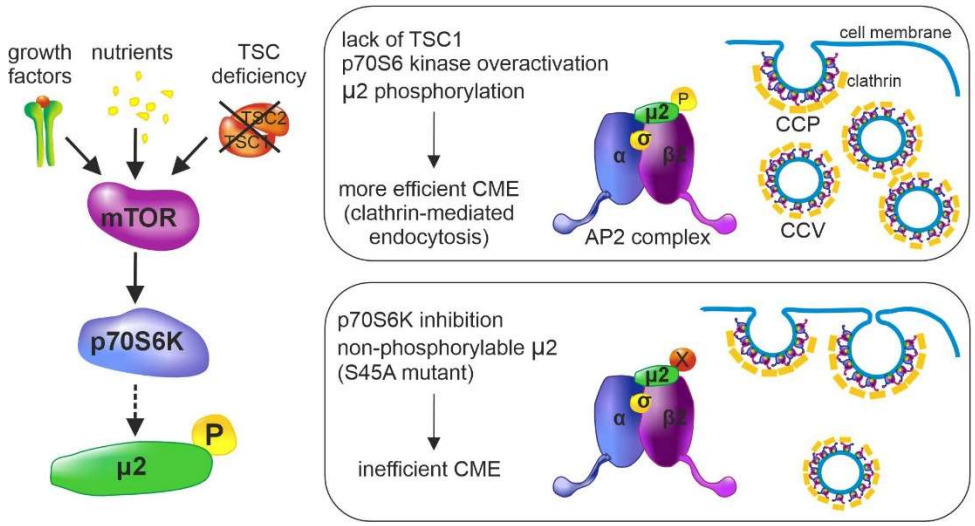

Figure 7. mTOR-p70S6K-AP2 axis regulates CME.

Summary of the main findings. High activity of the mTOR-p70S6 kinase pathway promotes the phosphorylation of the μ2 subunit of the AP2 adaptor complex, which is needed for efficient CME. Lack of the pathway's activity or substitution of the wild-type μ2 with the non-phosphorylable S45A μ2 mutant alters the early steps of CME.

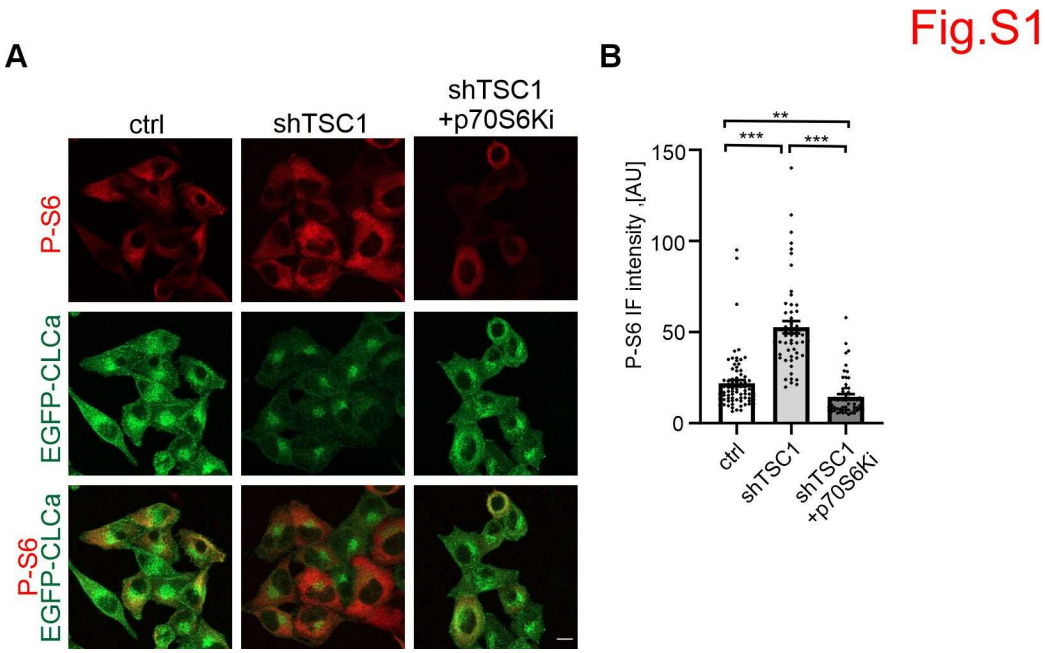

Figure S1. Treatment with p70S6Ki decreases P-S6 levels in HeLa cells.

A. Representative confocal images of immunofluorescent labeling of P-S6 (S235/236) (red) in HeLa cells stably expressing EGFP-CLCa (green) alone or together with TSC1 shRNA. Cells were serum-starved and treated for 2 h with 0,1% DMSO or 10 µM p70S6Ki. Scale bar = 10 µm **B.** Quantification of immunofluorescence signal of P-S6 (S235/236) normalized to cell area in cells treated as in *A*. The data are shown as the mean value ± SEM. $N = 2$ independent experiments. Number of analyzed cells (n) = 78 (ctrl), 54 (shTSC1), 58 (shTSC1 +p70S6Ki). ***$p < 0.001$, **$p < 0.01$ (Kruskal Wallis test [H=100.9] with Dunn's multiple comparisons test).

Fig.S2

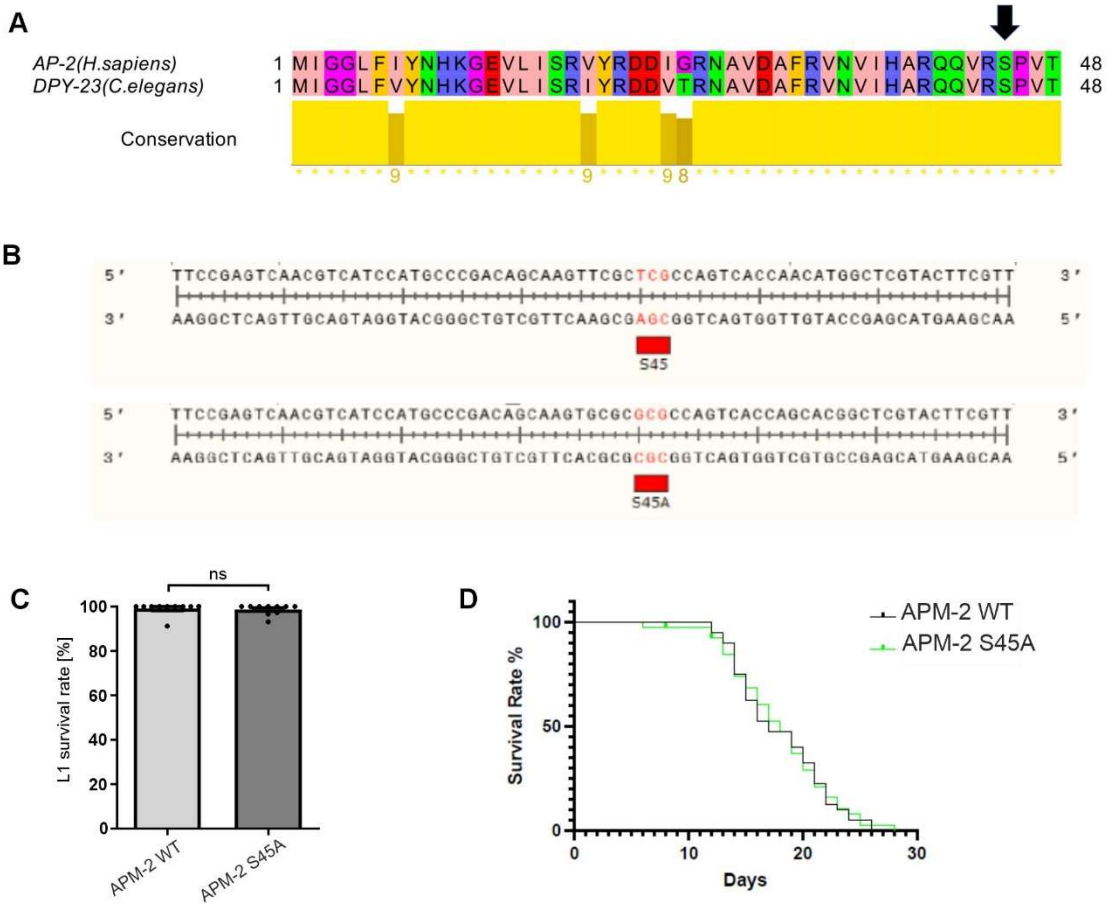

Figure S2. Serine 45 in APM-2 in *C. elegans.*

A. Global alignment of N-terminus of human AP-2 (UniProt ID: Q96CW1) and *C. elegans* DPY-23 (UniProt ID: P35603). Sequences were aligned using the EMBOSS Needle web server [67] with default parameters and visualized in the Jalview Desktop software [68] with residues colored by their physicochemical properties; the arrow indicates S45 position. **B.** Representative sequencing results for the R160.1b.1 locus in the wild-type (N2) strain (top section) compared with nematodes where the 375th position was edited to change T to C, resulting in the amino acid substitution to Ala45 (A). The data were examined using SnapGene 6 software (Insightful Science; snapgene.com). **C.** Percentage of hatched L1 larvae from eggs laid over 24 hours by wild type (N2) and apm-2 mutant strain. *ns* – non-significant (Mann–Whitney test). **D.** Lifespan comparisons of control (WT – wild type, N2) and APM-2S45A worms at 20°C. *ns* – non-significant (Mantel-Cox log-rank test).

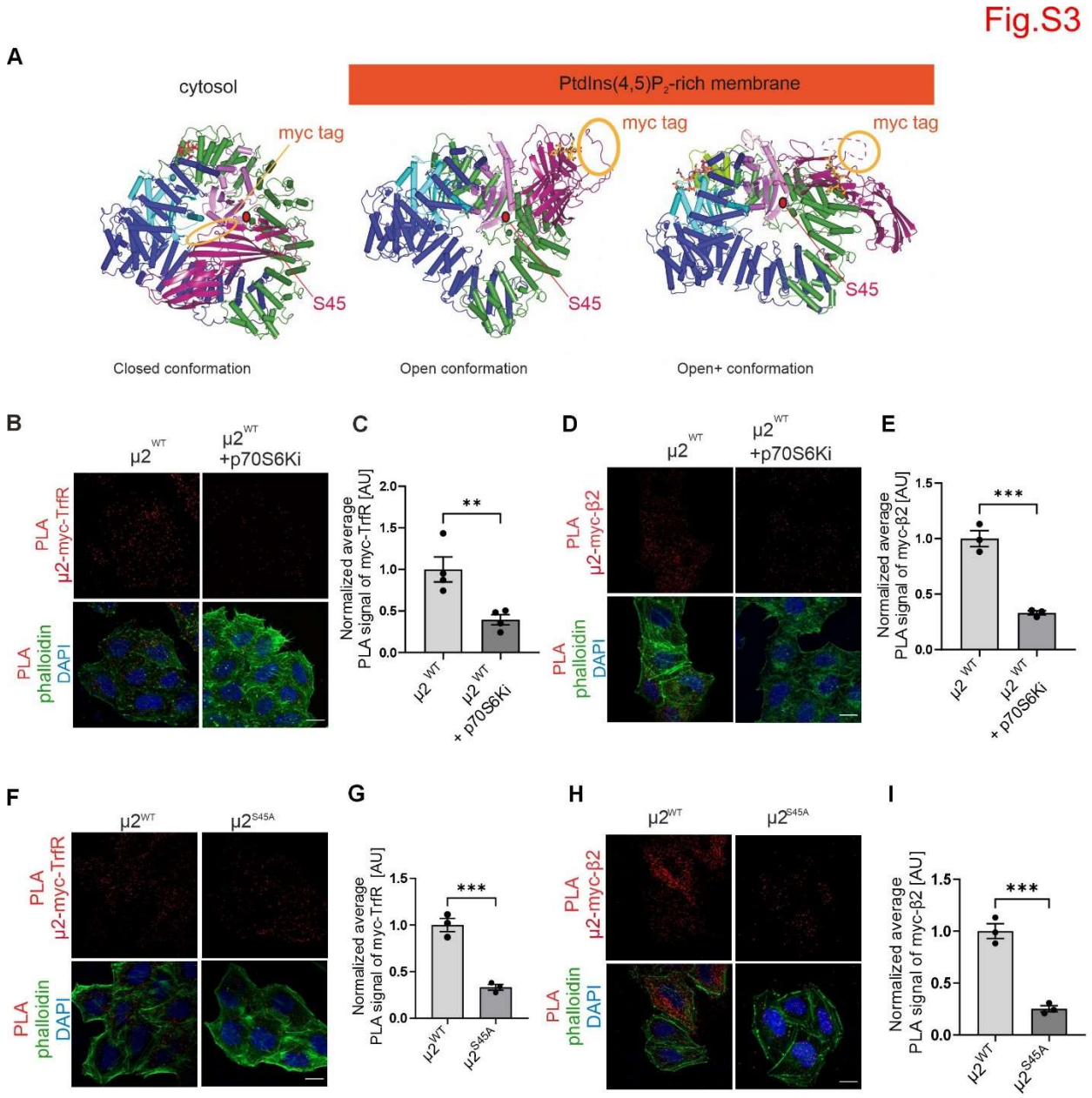

Figure S3. S45A substitution in μ2 affects conformational changes of AP2 complex.

A. Structures of AP2 core in closed cytosolic conformation (left, PDB ID 2vgl [1]) and in two membrane-binding conformations (views 'perpendicular' to the plasma membrane): open (center, PDB ID 2vgl, [2]) and open+ conformations (right, PDB ID 6QH6, [7]). Subunits of the complex are colored in blue (α), green (β2), cyan (σ2), and pink (Nμ2)/dark pink (Cμ2); the complex orientation at the membrane is based on the position of its cargo peptides [2,7]. Nμ2 Ser45 and the sites of myc-tag insertion into the Cμ2 subdomain are highlighted. **B.** Representative images of myc–TrfR PLA signals (red) in HeLa KO μ2 transfected with a plasmid encoding myc-μ2^{WT} and treated for 2 h with 0.1% DMSO or 10 μM p70S6Ki. Cells were fluorescently labeled with Alexa Fluor 488-conjugated phalloidin (green), and DAPI (nuclei, blue) Scale bar = 10 μm. **C.**

Quantification of the number of myc-TrfR PLA puncta in cells treated as in *B*. The data are expressed as the mean number of PLA puncta per cell, normalized to the control variant ($\mu2^{WT}$) ± SEM. N = 4 independent experiments. Number of analyzed cells (n) = 89 ($\mu2^{WT}$), 104 ($\mu2^{WT}$ + p70S6Ki), $^{**}p < 0.01$ (Student's t-test for independent samples; t = 4.151, df = 3). **D.** Representative images of myc–β2 PLA signals (red) in HeLa KO μ2 transfected with a plasmid encoding myc-$\mu2^{WT}$ and treated for 2 h with 0.1% DMSO or 10 μM p70S6Ki. Cells were stained with Alexa Fluor 488-conjugated phalloidin (green) and DAPI (nuclei, blue). Scale bar = 10 μm. **E.** Quantification of the number of myc-β2 PLA puncta in cells treated as in *D*. The data are expressed as the mean number of PLA puncta per cell, normalized to the control variant ($\mu2^{WT}$) ± SEM. N = 3 independent experiments. Number of analyzed cells (n) = 62 ($\mu2^{WT}$), 59 ($\mu2^{WT}$ + p70S6Ki), $^{***}p < 0.001$ (Student's t-test for independent samples; t = 9.616, df = 2). **F.** Representative images of myc–TrfR PLA signals (red) in HeLa KO μ2 transfected with plasmids encoding myc-$\mu2^{WT}$ or myc-$\mu2^{S45A}$. Cells were stained with Alexa Fluor 488-conjugated phalloidin (green) and DAPI (nuclei, blue). Scale bar = 10 μm. **G.** Quantification of the number of myc-TrfR PLA puncta in cells transfected as in *F*. The data are expressed as the mean number of PLA puncta per cell, normalized to the control variant ($\mu2^{WT}$) ± SEM. N = 3 independent experiments. Number of analyzed cells (n) = 60 ($\mu2^{WT}$), 53 ($\mu2^{S45A}$), $^{***}p < 0.001$ (Student's t-test for independent samples; t = 8.659, df = 4). **H.** Representative images of myc–β2 PLA signals (red) in HeLa KO μ2 cells that were transfected with plasmids encoding myc-$\mu2^{WT}$ or myc-$\mu2^{S45A}$. Cells were labeled with Alexa Fluor 488-conjugated phalloidin (green) and DAPI (nuclei, blue). Scale bar = 10 μm. **I.** Quantification of the number of myc-β2 PLA puncta in cells transfected as in *H*. The data are expressed as the mean number of PLA puncta per cell, normalized to the control variant ($\mu2^{WT}$) ± SEM. N = 3 independent experiments. Number of analyzed cells (n) = 62 ($\mu2^{WT}$), 56 ($\mu2^{S45A}$), $^{***}p < 0.001$ (Student's t test for independent samples; t = 9.592, df = 4).

Fig.S4

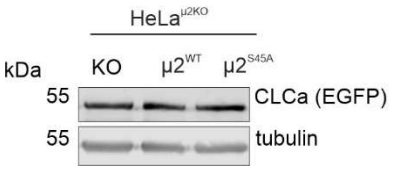

Figure S4. Expression of myc- $\mu2^{WT}$ or myc-$\mu2^{S45A}$ does not affect the levels of EGFP-CLCa.

Western blot showing level of EGFP-fused clathrin light chain (CLCa) and tubulin in HeLa KO μ2 cells stably expressing EGFP-CLCa and myc- $\mu2^{WT}$ or myc-$\mu2^{S45A}$.